Key Points:

- The Ivrea-Verbano Zone in the Italian Alps is a unique archive that allows studying otherwise inaccessible parts of the Earth's interior
- Calculated seismic wave speeds and rock densities indicate amphibole gabbros/pyroxene hornblendite as the best fit the geophysical observations of the Ivrea body
- The Ivrea body is the result of magmatic underplating producing mafic hydrous magmas forging a 45-km thick continental crust

Correspondence to:
M. Pistone,
Mattia.Pistone@uga.edu

Joint Geophysical-Petrological Modeling on the Ivrea Geophysical Body Beneath Valsesia, Italy: Constraints on the Continental Lower Crust

Mattia Pistone[1,2] , **Luca Ziberna[3,4]** , **György Hetényi[1]** , **Matteo Scarponi[1]**, **Alberto Zanetti[5]**, and **Othmar Müntener[1]**

[1]Institute of Earth Sciences, University of Lausanne (UNIL), Lausanne, Switzerland, [2]Department of Geology, University of Georgia (UGA), Franklin College of Arts and Sciences, Athens, USA, [3]Department of Mathematics and Geosciences, University of Trieste, Trieste, Italy, [4]Bayerisches Geoinstitut, University of Bayreuth, Bayreuth, Germany, [5]Institute of Geosciences and Earth Resources, IGG-CNR, Pavia, Italy

Abstract One of the few near-complete continental crustal sections exposed on Earth's surface is the Ivrea-Verbano Zone (Western Alps, Italy), which is considered as a petro-geophysical reference of the continental lithosphere. Exposed peridotite slivers embedded in lower crustal rocks at the surface and large density, seismic velocity anomalies of the Ivrea Geophysical Body in the subsurface suggest that mantle-like rocks are located as shallow as a few kilometers depth, but the actual composition of the rocks producing these anomalies is unknown. Here we investigate how the published seismological and new gravimetric data in the location of Valsesia could be reconciled with petrologic data and models of the Ivrea-Verbano Zone. We use the Perple_X software to calculate densities and compressional wave velocities for a range of possible deep crustal rock types. We argue that amphibole gabbros (<18 km depth) and pyroxene hornblendites (>18 km depth) provide the best fit to the joint geophysical and petrologic constraints, whereas residual ultramafic rocks and anhydrous gabbros are inconsistent with the existing data. This indicates that the Ivrea Geophysical Body beneath the Valsesia area in the Ivrea-Verbano Zone preserves the structure of an igneous complex formed during magmatic underplating from the crystallization of hydrous mafic magmas. This would imply melting of a damp mantle source that produced a continental crust of an original thickness of up to ∼48 km in the Permian, of which ∼30 km are exposed at Earth's surface today.

Plain Language Summary Geophysical imaging and surface geology provide essential insights into the Earth's outer skin: the crust and the upper mantle. The Ivrea-Verbano Zone in the Italian Alps is a unique archive that allows studying otherwise inaccessible parts of the Earth's interior. Here, we investigate the composition of the deep roots of the Ivrea-Verbano Zone—the Ivrea body— using a combination of published laboratory data on rock physical properties, published and new geophysical data, and thermodynamic modeling along an idealized vertical "borehole" in the core of the area. Calculated seismic wave speeds and rock densities suggest that amphibole gabbros and pyroxene hornblendites are the hydrous rock types that best fit the geophysical observations of the Ivrea body. Hence, the Ivrea body has mafic composition as a result of magmatic underplating, determined by the ascent of mantle-derived hydrous magmas. This combination of geophysical and petrological data is important to find the properties and history of this region, and can be critical in unraveling the composition of other buried geological structures causing geophysical anomalies worldwide.

1. Introduction

Exposed crust-mantle sections are essential archives of the past and contemporary lithosphere (Rudnick & Fountain, 1995; Rudnick & Presper, 1990; Percival et al., 1992) and are fundamental for estimates of the composition of the Earth's crust (Rudnick & Gao, 2003) above the Mohorovičić discontinuity or Moho separating the Earth's crust from the subjacent mantle (Mohorovičić, 1910). While the "geophysical Moho" defines the sudden change in compressional wave velocities from typically <7 km/s to >8 km/s, the "petro-logical Moho" transition zone corresponds to the level where plagioclase disappears from the crystallizing assemblage within the cumulates of underplated mafic magma (Müntener & Ulmer, 2006). The "petrological
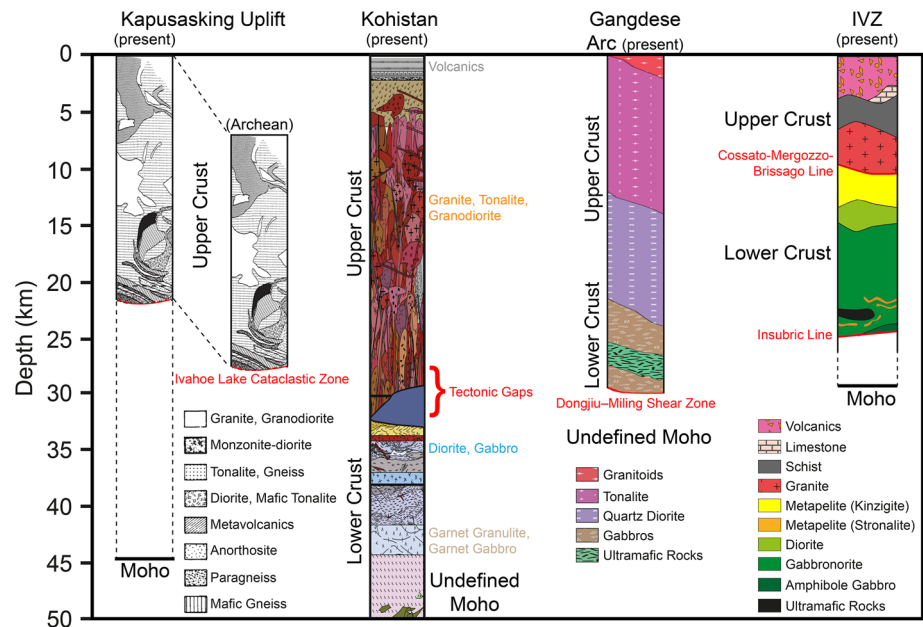
Figure 1. Representative crustal cross-sections of the Archean and present-day Kapuskasing Uplift (Ontario, Canada; after Fountain et al., 1990), present-day Kohistan Arc, including the Southern Plutonic Complex, Chilas Complex, and Gilgit Complex (Himalaya, Pakistan; after Jagoutz, 2014), Gangdese Arc (after Guo et al., 2020), and the Valsesia sector of the Ivrea-Verbano Zone (IVZ; Western Alps, Italy). Ruled area provides an estimate of the amount of lower continental crust not exposed in these representative cross-sections. Tectonically excised sections are caused by faults and shear zones (highlighted with red lines). The vertical axis reporting reconstructed depth of the exposed crustal sections is drawn to scale and all units to the thickness derived from geobarometric constraints.

Moho" then corresponds to the disappearance of feldspar in the downward gradation of gabbroic cumulates to ultramafic cumulates as observed in ophiolite and arc sections (Bowes, 1989; Burg et al., 1998). In the exposed crust-mantle sections, it is possible to apply a thorough investigation of spatial and temporal relationships between lower crustal rock units and even with the upper crust, which cannot be obtained by xenolith investigations alone. For example, processes of mafic magmas emplaced at the Moho and in the lowermost crust (magmatic underplating) linked to upper crustal processes including volcanism can only be studied in a few cross-sections worldwide, most of which are incomplete (only half to two-third of such crustal sections outcrop on the surface) and none of them display a complete Moho transition zone (Salisbury & Fountain, 1990; Figure 1). Among the known non-Archean crustal cross-sections with continental (e.g., Sila Massif, Calabria, Italy; Prince Rupert, British Columbia, Canada; Doubtful Sound, Fiordland, New Zealand) and paleo-island arc signature (e.g., oceanic arcs: Kohistan, Pakistan; Talkeetna, Alaska, USA; continental arcs: Sierra de Famatina, Argentina; Gangdese, southern Tibet, China), the Ivrea-Verbano Zone (IVZ; Western Alps, Italy) is a type locality for studying the continental crust from its base to the surface (Henk et al., 1997; Salisbury & Fountain, 1990; Spicher, 1968).

1.1. The IVZ

The IVZ was the first terrain identified as an exposed cross-section of the continental crust (Schweizerische Mineralogische und Petrographische Mitteilungen, v. 48, no. 1, 1968). The deepest rocks of the IVZ are granulite facies metasediments and metabasites intercalated with intrusive mafic rocks, and mantle peridotite slivers embedded in lower crustal rocks (Brodie & Rutter, 1987; Fountain, 1989; Quick et al., 1995; Zingg, 1990; Figures 1 and 2). The Paleozoic basement of the IVZ records protracted, polyphase tectonic history. After crustal amalgamation and accretion during the Devonian and Carboniferous Variscan phases (von Raumer et al., 2013), the continental lithosphere underwent a major reorganization during the late Carboniferous and early Permian during which the continental crust is thought to have reached a thickness of 30–35 km (Petri et al., 2017). Extensional tectonics along with mantle-derived magmatic intra
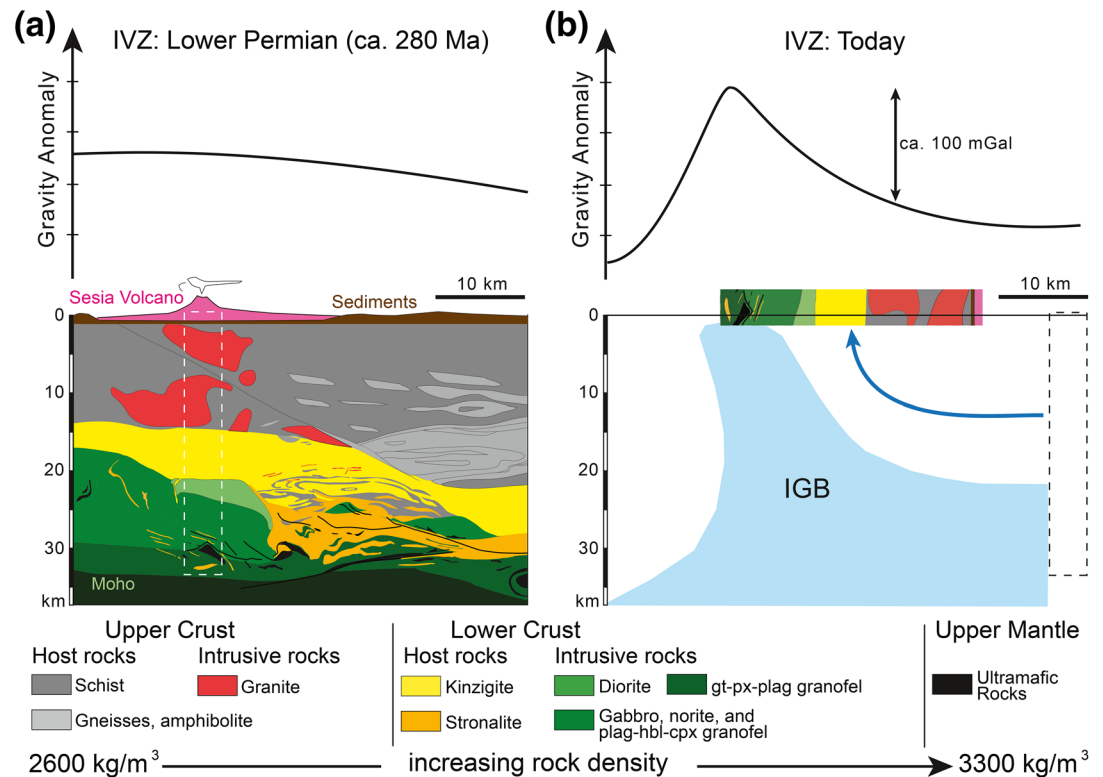
Figure 2. (a) Lower Permian section of the IVZ (modified after Brack et al., 2010) with a low-amplitude gravity anomaly, drawn schematically, for average continental crust thickness (~35 km; Christensen & Mooney, 1995). (b) The tilting of the IVZ column during Alpine orogenesis (indicated by blue arrow) brought the IGB at shallow depth, causing a large (~100 mGal) positive gravity anomaly above the shallow IGB (Scarponi et al., 2020), and made the IVZ a worldwide unique place. Legend: IVZ lithologies arranged according to the increasing rock density from upper crust (~2,600 kg/m³) to upper mantle (~3,300 kg/m³) (Khazanehdari et al., 2000). IGB, Ivrea Geophysical Body; IVZ, Ivrea-Verbano Zone.

and underplating favored the differentiation of the continental crust and drove the metamorphic events from granulite and amphibolite facies rocks in the lower crust to greenschist facies rocks in the upper crust (Schuster & Stüwe, 2008). The major tectonic extensional fault is the Cossato-Mergozzo-Brissago Line, which is a high-temperature shear zone that was active during Permian magmatism (Snoke et al., 1999).

After Permian magmatism, and prior to Alpine shortening, the South-Alpine crust underwent considerable thinning during early Mesozoic rifting before it became part of the southern passive margin of the Tethys opening to the west and north (Bertotti, 1991; Bertotti et al., 1993; Sanders et al., 1996). Specifically, radiometric cooling ages show that the Pogallo Line is a pre-Alpine fault zone that was active during Late Permian to Early Jurassic times (Boriani & Sacchi, 1973; M. R. Handy, 1987; M. R. Handy & Zingg, 1991; Mulch et al., 2002; Zingg, 1983). Tilted back into its pre-Alpine position, the Pogallo Line appears as an east-dipping low angle fault along which part of the Mesozoic extension was accommodated (Hodges & Fountain, 1984). It is estimated that crustal attenuation and rifting during Late Proterozoic and Early Mesozoic time thinned the crust to a thickness of 10–20 km (M. R. Handy & Zingg, 1991). Other authors favor that the Pogallo Line was already steep in the Permian (Boriani & Sacchi, 1973). The Strona Ceneri Zone and the IVZ have been collectively interpreted as a more or less coherent section through the pre-Alpine continental crust (Brack et al., 2010; Schaltegger & Brack, 2007) that progressively exposes deeper crustal levels to the northwest (Fountain, 1976). According to this hypothesis, middle and upper crustal levels are exposed in the Strona Ceneri Zone, and lower crustal levels are exposed in the IVZ. Within the latter, metamorphic grade and equilibration pressures increase from amphibolite grade (~0.4 GPa) to granulite grade (~0.9 GPa) near the Insubric Line (Demarchi et al., 1998; Henk et al., 1997; Zingg, 1983). In the southern IVZ, foliation and compositional layering are subvertical and isobars are approximately subparallel to the Insubric Line (Demarchi

et al., 1998). Therefore, the IVZ is viewed on the geological map as a subvertical cross section through the pre-Alpine deep crust, that has been tilted along a north-northeast axis (Figure 2b).

Several studies have shown that the post-Permian evolution of the IVZ was affected, at least locally, by pulses of rifting-related magmatism, fluid influx, and heating in the late Triassic and Jurassic (Ewing et al., 2015, 2013; Grieco et al., 2001; Mazzucchelli et al., 2010; Schaltegger et al., 2015; Smye et al., 2019; Stähle et al., 1990; Zanetti et al., 2013). These results do not support models of continuous conductive cooling following peak temperatures associated with the intrusion of the Mafic Complex during the early Permian (M. Handy et al., 1999; Siegesmund et al., 2008; Wolff et al., 2012). During the Jurassic continental breakup and opening of the Piemont-Liguria ocean the IVZ experienced local peak temperatures of 550°C–660°C (Ewing et al., 2015) to ~700°C (Smye et al., 2019). These thermal perturbations were modeled by Smye et al. (2019) and indicate that the IVZ achieved a near steady-state continental geotherm around 100 Ma. A temperature <300°C is considered for the IVZ during final exhumation during Alpine orogenesis.

The preservation of the IVZ pre-Permian and early Permian section is evidenced by the near-isobaric cooling following Permian magmatism and associated contact metamorphism (Müntener et al., 2000; Petri et al., 2016) and the Triassic fluvial to shallow-marine stratigraphic record (Petri et al., 2019). The two major tectonic lineaments Cossato-Mergozzo-Brissago Line (SW sector of the IVZ) and Pogallo Line (NE sector of the IVZ) divide the lower and upper crust of the present-day IVZ section in its southeastern and northwestern sector, respectively (Bertotti et al., 1993; M. R. Handy, 1987). Almost complete sections of the continental crust are preserved, with limited post-Permian exhumation and thinning of the continental lithosphere (Demarchi et al., 1998; M. R. Handy, 1987; M. R. Handy & Zingg, 1991; Mulch et al., 2002; Petri et al., 2019; Redler et al., 2012; Schmid et al., 1987). Therefore, despite the protracted, polyphase tectonic history, the exhumation of the IVZ offers, by far, the most complete continental crustal section in the world (Figures 1 and 2).

1.2. The Ivrea Geophysical Body

The so-called Ivrea Geophysical Body (IGB) refers to rock masses which cause well-known and pronounced geophysical anomalies extending over 200 km along the inner arc of the Western Alps, the northeastern third of which is below the exposed IVZ (Figures 3a and 3b). The IGB served as a calibrating benchmark in search of other crustal sections in the world (e.g., Brooks, 1970; Forman & Shaw, 1973; Gibb & Thomas, 1976). Geophysical investigations across various sections of the IGB (Ansorge, 1968; Ansorge et al., 1979; Kissling, 1993; Ménard & Thouvenot, 1984; Niggli, 1946; The ECORS-CROP Gravity Group, 1989; Vecchia et al., 1968) indicate that this body causes distinct gravimetric, magnetic, and seismic anomalies, which have varying strength and also relative position with respect to each other along the full length of the IGB. While the velocity and density anomalies may typically overlap, as in the early synthesized model of Berckhemer (1968, 1969) based on gravity data and active seismic refraction data over long distances, magnetic anomalies may be spatially distinct (Lanza, 1982). Nevertheless, all studies seem to suggest that dense rocks of the lower continental crust and upper mantle are located at unusually shallow depth and cause the largest positive gravity anomaly in the Alps (Béthoux et al., 2007; Kissling, 1980, 1984; Masson et al., 1999; Paul et al., 2001; The ECORS-CROP Gravity Group, 1989; Thouvenot et al., 2007; Vernant et al., 2002; Figure 2). Therefore, the IGB is interpreted as a piece of the Adriatic lithosphere (Schmid et al., 1987, 2004, 2017) brought to shallow depths as a consequence of exhumation processes during the Alpine orogenic cycle (Figure 2; Rey, 1990). The northeastern third of the IGB extends from Locarno in southern Switzerland to the town of Ivrea, with exposed rocks on the surface (the IVZ) and relatively shallow depth as the source of the anomalies, while further to the south-southwest and to the Ligurian Sea, the IGB is located at relatively greater depths and without corresponding exposure at the surface (Figures 3a and 3b).

The location and depth of local maxima of the IGB vary with published models (de Franco et al., 1997; Kissling, 1993; Solarino et al., 1997, 2018). The classically known "Bird's Head" model of Berckhemer (1969) indicated ~3 km depth below sea level, mostly from gravity as the seismic data is sparse and averaged over long distances. Locally, in the Valsesia, recent 3D density modeling fitting new gravity data suggest the top of the density anomaly at 1 ± 1 km depth below sea level (Scarponi et al., 2020; Figures 2 and 3). The various gravity models seem to agree on the amplitude of the density anomaly at about 400 kg/m^3 (400 kg/m^3 in Berckhemer, 1968; 350 kg/m^3 in Kissling et al., 1984; 360–410 kg/m^3 in Bürki, 1990; 400 ± 100 kg/m^3
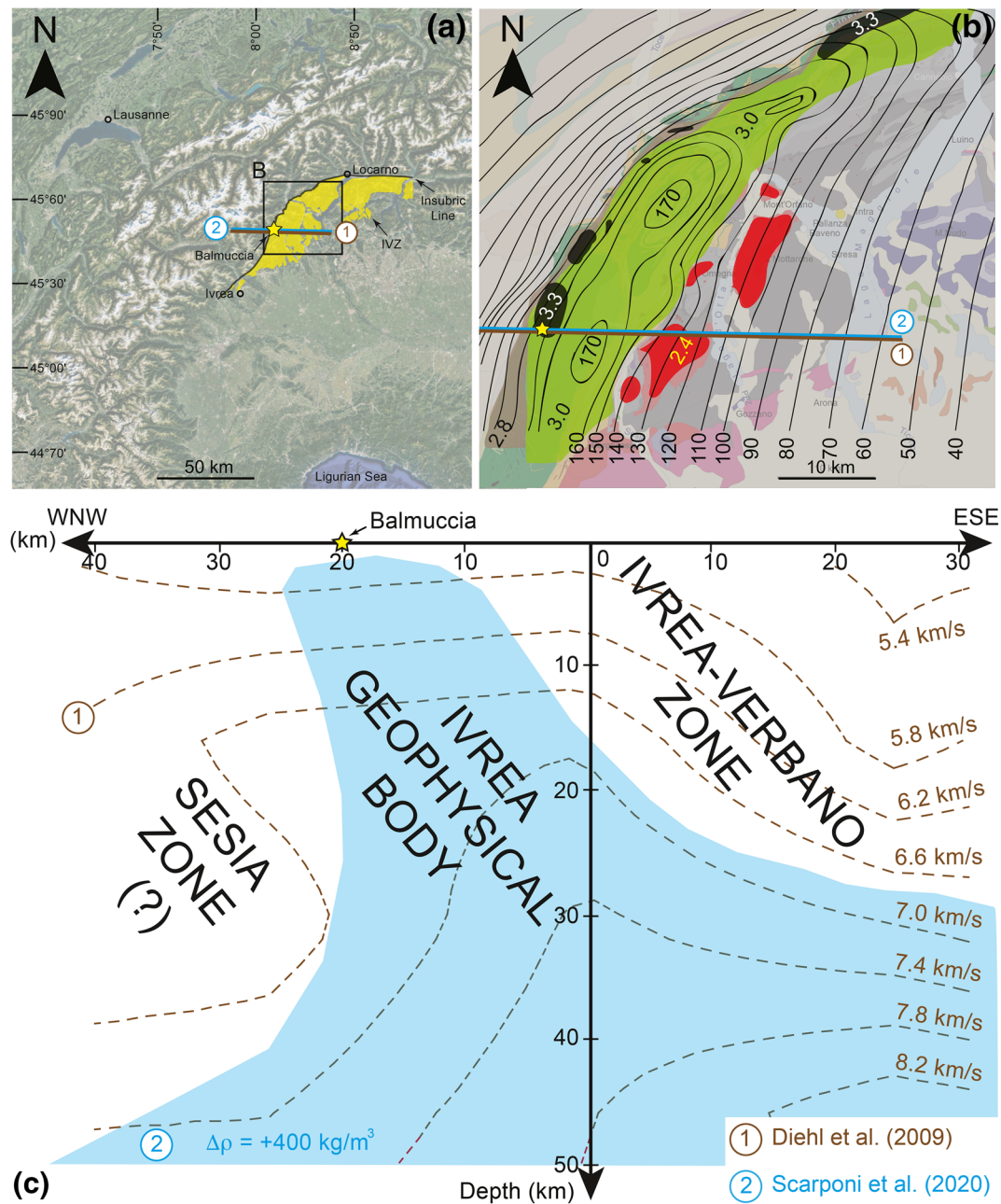
Figure 3. (a) Location of the profiles of Diehl et al. (2009) (brown solid line, projected and centered in Balmuccia, highlighted by the yellow star), and Scarponi et al. (2020) (light blue solid line) on the top of a satellite map reporting the location of the IVZ (yellow area). (b) Map showing the bulk density (g/cm^3) distribution of surface rocks (red = granites, light green = IVZ, black = ultramafic rocks, brown = Insubric Line) and calculated gravity effect of the IGB (black contours with gravity values in mGal) in the IVZ (redrawn after Kissling, 1984 and superimposed on the geological map of Brack et al., 2010). (c) Cross-section of the shallow IGB along the profiles marked solid lines in (a) and (b), as determined by gravity anomalies in light blue arrow with density contrast of 400 ± 100 kg/m^3 from gravimetric modeling (Scarponi et al., 2020). Brown dashed lines are isovelocities projected from local earthquake tomography at 25 × 25 (horizontal) × 15 (vertical)-km spatial resolution (interpolated from Diehl et al., 2009). At surface: the yellow star indicates the location of Balmuccia. IGB, Ivrea Geophysical Body; IVZ, Ivrea-Verbano Zone.
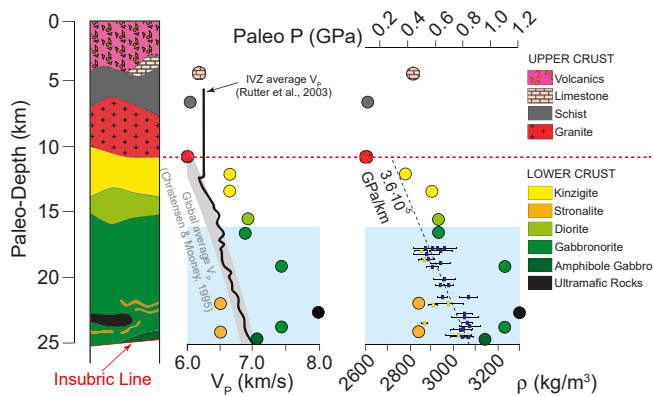
Figure 4. Schematic lithological, seismic (compressional P waves: V_P), and density (ρ) properties of bulk rocks from the IVZ as a function of paleo-depths (≈distances from the Insubric Line). Lithological data are from James (2001), Quick et al. (2003), Sinigoi et al. (2011), and Klötzli et al. (2014). V_P and ρ data of the IVZ rocks are arranged according to their location of sampling and are from Khazanehdari et al. (2000). V_P and ρ data symbols are correlated to the specific lithologies described in the legend. The average V_P gradient along the IVZ section is from Rutter et al. (2003). Gray band shows global average V_P-depth relation for continental crust (Christensen & Mooney, 1995). Geobarometric constraints based on mineral assemblages from IVZ metamorphic (blue squares) and igneous rocks (yellow squares) allow the estimation of the paleo-pressures (P) of the IVZ lower crustal domain, with the reconstruction of the paleo P gradient (black dashed line) in Valsesia (Demarchi et al., 1998; M. Handy et al., 1999; Henk et al., 1997; Petri et al., 2019). Light blue areas indicate the V_P and ρ data of the IVZ rocks considered in the thermodynamic calculations in this study. IGB, Ivrea Geophysical Body; IVZ, Ivrea-Verbano Zone.

in Scarponi et al., 2020; Figure 3). In map view, the locations of the proposed maxima (Scarponi et al., 2020) and where the Adriatic Moho seismically "vanishes" roughly follow the Insubric Line (western Periadriatic Seam; Gansser, 1968), the former Europe-Adria suture (Schmid & Kissling, 2000) within a distance of ~15 km. The Adriatic Moho reaches ~40–45 km depth, possibly dipping north to northeast (Lombardi et al., 2008; Spada et al., 2013).

In terms of seismic velocity anomalies, lateral variations along the strike of the IGB can be inferred from differences between two-dimensional profiles (Nicolas et al., 1990; Solarino et al., 1997; The ECORS-CROP Deep Seismic Sounding Group, 1989). A better insight can be gained from the recent three-dimensional local earthquake tomography model in terms of P-wave velocity (V_P) (Diehl et al., 2009), which shows the IGB roots to extend to depths of 45 km, and the shallowest high-velocity signal as shallow as 12–15 km along a significant length of the Western Alps, similar to observations of the ECORS-CROP and NFP-20-West geological-geophysical transects (Nicolas et al., 1990; The ECORS-CROP Deep Seismic Sounding Group, 1989). However, the spatial resolution of this seismic tomographic grid (25 × 25 × 15 km) presented by Diehl et al. (2009) is one order of magnitude larger than the current scale of interest in the IVZ and, inherently, images bulk V_P variations. Therefore, this model does not sufficiently resolve sharp seismic interfaces at local scale (at the km scale) as evidenced by the discrepancy with respect to density models based on gravity data. Furthermore, instead of a "normal" upper mantle V_P of 8 km/s, the shallow portion of the IGB shows values closer to 7 km/s (Figure 3), which has been suggested to result from a partially serpentinized (30–60 vol.%) mantle body with a density of 3,000–3,200 kg/m^3 (Zhao et al., 2015). The present-day coverage of the seismological data set is mainly limited by the quality of available waveform data in the Alpine region (Diehl et al., 2009). Available shear wave velocity (V_S) models based on observations of seismic ambient noise capture larger scale, crustal to lithospheric structures with relatively coarse spatial resolution (Kästle et al., 2018; Y. Lu et al., 2018; Molinari et al., 2015; Stehly et al., 2009) that do not allow for detailed, kilometer-scale imaging of the IGB at depth.

These geophysical observations make the IVZ and its root zone represented by the IGB unique in the world to evaluate the composition and structure of the continental crust and the processes that forged it. This can be done by correlating petrologic composition and physical properties of the lower crustal rocks to the observed geophysical signals at the location of Valsesia. To this goal, we calculate the density and seismic velocity structure for a series of typical rocks from the IVZ to a depth of 50 km and combine them with available petrophysical data. An analysis of various density-velocity depth-structure profiles of the IVZ indicates that amphibole gabbros provide the closest fit for the currently available geophysical constraints on the IGB.

2. Methods

To unravel the plausible rock composition(s) of the IGB, we use a combination of published laboratory-measured seismic compressional wave velocities (V_P) and densities (ρ) of lower crust and upper mantle rocks (Figure 4) together with thermodynamic calculations of V_P and ρ run using the Perple_X set of computer programs (Connolly, 1990, 2005). The setting for our calculations is along a virtual 1-D vertical profile in Valsesia, below which the geophysical discontinuity is proposed as shallow as ~1 km depth below sea-level based on the latest three-dimensional density model of Scarponi et al. (2020) (Figure 3). The calculations start from a depth of 3 km, which is consistent with the minimum pressure of laboratory measurements (Khazanehdari et al., 2000) and within the IGB below the 1 ± 1 km discontinuity of the recent gravity model (Scarponi et al., 2020). Here we assume that the IGB was emplaced to its current depth after an exhumation corresponding to 0.5 GPa (Figure 2) below 700°C (Ewing et al., 2015; Smye et al., 2019) using

an average continental geotherm (Christensen & Mooney, 1995), which allowed the original lithologies to remain "frozen" while emplaced to shallow depth. The pressure decrease with the IVZ uplift is an upper bound based on the 10 Ma old apatite fission-track ages (Wagner & Reimer, 1972) and tectonic reconstructions (Schmid et al., 2004). No in situ geothermal gradient constraints and deep-reaching heat flow data related to the IVZ and IGB are available up to date.

The petrophysical data set is from Khazanehdari et al. (2000), who performed laboratory-based V_P and ρ measurements on a suite of oriented rock samples of the IVZ (Figure 4) from 25°C to 700°C and from 0.1 to 0.55 GPa (corresponding to a depth range of 3–15 km depth, which do not correspond to the paleo-depth of the IVZ rocks). The suite of rocks here considered represent most of the volume of the primitive (high Mg#) magmatic rocks composing the IVZ lower crust: amphibole gabbro from Val Sessera, olivine gabbro from Valsesia, and pyroxenite and lherzolite from the Balmuccia Massif (Table 1). Along with this data set, we also consider the V_P measurements on peridotite (harzburgite) with different degrees of serpentinization collected during International Oceanic Drilling Program missions (Carlson & Miller, 2003; Christensen, 1966; Miller & Christensen, 1997). While we have solid laboratory constraints that account for the effect of porosity (porosity-pressure hysteresis; Jerauld & Salter, 1990), mineral texture, and rock microstructure on V_P for the depth range 0–15 km, this is not the case for greater (paleo-)depths. We therefore performed phase equilibrium calculations to explore the mineralogy, density, and seismic wave velocities of the IGB covering a wide range of plausible models described below.

We use the software package Perple_X (Connolly, 1990, 2005; version 6.8.1) to compute stable mineralogy and phase diagrams (i.e., pseudosections; Connolly & Petrini, 2002) as a function of P-T for each composition by Gibbs free energy minimization (Connolly, 2009). From the results, we extract the petrophysical properties of the rock (V_P and ρ) obtained by averaging schemes such as Voigt-Reuss-Hill. Two sets of thermodynamic databases, labeled as STX11 and HP02, are used. STX11 includes the data set of end-member properties and solid-solution models for olivine, pyroxenes, plagioclase, spinel, and garnet of Stixrude and Lithgow-Bertelloni (2011). It has been applied to the bulk compositions of anhydrous lherzolite, dunite, and pyroxenite (websterite, clinopyroxenite, and bronzitite) of Balmuccia Massif (Hartmann & Wedepohl, 1993), primitive "cumulate" olivine gabbro from the Lower Mafic Complex from Valsesia (Rivalenti et al., 1975) and external gabbros of Finero from Val Cannobina (Table 1). The HP02 database includes the data set of end-member properties of Holland and Powell (1998) and solid-solution models for olivine—O(HP), garnet—Gt(HP) (Holland & Powell, 1998), pyroxenes—Cpx(HP) and Opx(HP) (Holland & Powell, 1996), plagioclase—Pl(I1,HP) (Holland & Powell, 2003), spinel—Sp(HP) (Jamieson & Roeder, 1984), and amphibole—Amph(DHP) (Dale et al., 2000), and augmented with elastic moduli from Hacker and Abers (2004) and Jagoutz and Behn (2013), permitting the computation of seismic wave velocity. This thermodynamic model has been applied to the hydrous compositions of Finero Amphibole Peridotite (average crustal lherzolite; Zanetti et al., 1999), Finero Phlogopite Peridotite (average mantle lherzolite; Zanetti et al., 1999), Finero amphibole gabbro, and Sessera amphibole gabbro (Table 1). The H_2O content in both the peridotite and the gabbro is consistent with the maximum volumetric amount of amphibole found in the Finero peridotite (25 vol.%; Tommasi et al., 2017; Zanetti et al., 1999), Sessera gabbro (50 vol.%; Khazanehdari et al., 2000) and Finero gabbro (50 vol.%; Cawthorn, 1975), respectively, and consistent with the maximum volumetric amount of phlogopite found in the Finero peridotite (5 vol.%; Zanetti et al., 1999). Using the Finero gabbro and the Lower Mafic Complex olivine gabbro/gabbro, both devoid of hydrous phases as testing compositions, we inspected the potential differences of results given by the application of STX11 and HP02 databases. In the 9–21 km depth range, the maximum discrepancies between the two models are $\Delta V_P < 0.3$ km/s and $\Delta\rho < 140$ kg/m^3, with STX11 providing higher V_P and ρ values than HP02. Such discrepancies are related to the slightly different mineralogy and modal compositions predicted by the two models. However, typical values of V_P and ρ are smaller by about one-third between STX11 and HP02 databases. Rock types and compositions here considered are listed in Table 1.

To assess model uncertainties of V_P and ρ, petrophysical constraints by Perple_X are compared with rock V_P and ρ calculations using the model of Abers and Hacker (2016). This latter model decomposes solid solutions into pure end-member components (e.g., 100% plagioclase = X% anorthite + X% albite) and then applies Voigt-Reuss-Hill and Hashin-Shtrikman averages on the pure minerals. The end-member components are derived from Perple_X calculations as explained above and then used in the model of Abers and

Table 1

Average and Specific Bulk Compositions of the Representative Exposed Primitive Rocks of the Deep Lower Crust and Upper Mantle of the Ivrea-Verbano Zone (Balmuccia and Lower Mafic Complex in Valsesia, Finero in Val Cannobina, and Sessera River in Val Sessera) Used for the Perple_X Calculations Using the Two Thermodynamic Models STX11 and HP02

Reference	a	b	c	c	d	e	c	e	c	c	f	g	h	h	i	f
IVZ Valley	Sesia	Sesia	Sesia	Sesia	Sesia	Sesia	Sesia	Sesia	Sesia	Sesia	Sesia	Cannobina	Cannobina	Cannobina	Cannobina	Sessera
IVZ Location	Balmuccia	Balmuccia	Balmuccia	Balmuccia	Balmuccia	Balmuccia	Balmuccia	Balmuccia	Balmuccia	Balmuccia	Balmuccia	Finero	Finero	Finero	Finero	Sessera River
Rock	Lherzolite	Lherzolite	Pyroxenite	Pyroxenite	Pyroxenite Aug Pyrox.	Di Pyrox.	Pyroxenite	Dunite	Ol Gabbro L. Mafic C.	Ol Gabbro L. Mafic C.	Gabbro L. Mafic C.	Am Harzburgite	Am Lherzol.	Phl Lherzol.	Gabbro	Am Gabbro
Sample ID	FE37	Average	IV35	GZ8	Average	Average	Average	Average	IV117	IV301	Average	Average	Average	Average	Average	Average
SiO_2	43.51	47.23	43.20	44.80	47.23	51.77	46.34	39.66	45.30	47.00	47.11	44.00	40.46	43.17	45.81	44.04
TiO_2	0.06	0.54	0.44	0.61	0.54	0.22	0.40	0.02	1.21	0.93	1.18	0.03	0.04	0.06	2.57	1.54
Al_2O_3	0.64	11.24	5.20	7.30	11.24	4.26	4.77	0.50	11.00	16.80	19.75	1.23	2.22	1.39	14.20	19.68
Cr_2O_3	-	0.00	-	-	0.00	0.15	0.00	0.48	-	-	0.00	0.44	0.09	0.00	0.01	0.00
FeOTOT	10.25	7.73	12.18	13.41	7.73	5.88	9.26	8.63	10.44	7.39	9.95	7.09	12.30	7.94	14.62	10.29
MnO	0.21	0.15	0.20	0.22	0.15	0.14	0.15	0.14	0.20	0.13	0.17	0.13	0.15	0.12	0.24	0.13
NiO	-	0.00	-	-	0.00	0.02	0.00	0.36	-	-	0.00	0.31	0.06	0.00	0.00	0.00
MgO	41.57	19.83	32.78	27.35	19.83	24.69	25.62	49.87	14.10	13.98	7.90	44.00	43.17	45.73	8.10	9.08
CaO	2.54	12.40	3.80	4.29	12.40	12.54	12.93	0.33	15.93	11.84	11.31	1.28	1.25	1.19	11.98	13.37
Na_2O	0.04	0.81	0.34	0.23	0.81	0.30	0.44	0.02	0.74	2.30	2.11	0.11	0.22	0.16	1.97	1.56
K_2O	0.00	0.03	0.01	0.00	0.03	0.01	0.06	0.00	0.01	0.02	0.34	0.08	0.03	0.20	0.24	0.19
P_2O_5	0.04	0.03	0.01	0.01	0.03	0.02	0.04	0.00	0.01	0.02	0.18	0.01	0.01	0.04	0.25	0.11
Total	98.86	100.00	98.16	98.22	100.00	100.00	100.00	100.00	98.94	100.41	100.00	98.71	100.00	100.00	100.00	100.00
H_2O	0.00	0.00	0.00	0.00	0.00	0.00	0.00	0.00	0.00	0.00	0.00	0.50	0.50	1.00	0.00–1.00	1.00
Mg#	0.88	0.82	0.83	0.78	0.82	0.88	0.83	0.91	0.71	0.77	0.59	0.92	0.86	0.91	0.50	0.61
Model	STX11	STX11	STX11	STX11	STX11	STX11	STX11	STX11	STX11-HP02	STX11-HP02	STX11-HP02	HP02	HP02	HP02	STX11-HP02	HP02
Scenario	2	2	2	2	2	2	2	2	3	3	3	2	4	4	3	4
In	✓	✗	✗	✗	✗	✓	✗	✓	✓	✗	✗	✓	✗	✓	✓	✓
Figure 5																

Notes. Mn, Ni, P, and Cr were not used for the Perple_X calculations. Mg# is calculated as Mg/(Mg + Fe) (mole fractions). Symbols in the last row indicate the rock compositions that are reported (✓) and not reported (✗) in Figure 5. Average compositions are normalized to 100 wt.% on a volatile-free basis; specific compositions report original totals and H_2O contents estimated based on the volumetric proportions hydrous minerals (amphibole and phlogopite) at the scale of the bulk rock.

[a]Voshage et al. (1990). [b]Voshage et al. (1990). [c]Shervais and Mukasa (1991); Hartmann and Wedepohl (1993); Rivalenti et al. (1995); Mukasa and Shervais (1999). [d]Pin and Sills (1986). [e]Pin and Sills (1986). [f]Shervais and Mukasa (1999). [g]Shervais and Mukasa (1991); Mukasa and Shervais (1999). [h]Coltorti and Siena (1984). [i]Siena and Coltorti (1989); M. Lu et al., 1997a, 1997b; Stähle et al. (2001).

Hacker (2016). The two models provide the same V_P and ρ within 0.2 km/s and 150 kg/m^3 for end-member mineral compositions, respectively.

Our thermodynamic calculations do not include the effect of porosity, mineral texture, rock microstructure, or anisotropy on V_P (Almqvist & Mainprice, 2017). This limitation does not, however, affect our calculations because seismic anisotropy of the IVZ decreases systematically with depth, from the schistose upper crust (i.e., Serie dei Laghi, <20% anisotropy; Fountain, 1976) to the strongly "isotropic" rocks of the deep crust and upper mantle (<5% anisotropy; Barberini et al., 2007; Barruol & Kern, 1996; Barruol & Mainprice, 1993; Burke & Fountain, 1990; Burlini & Fountain, 1993; Khazanehdari et al., 2000; Rutter et al., 2003). Moreover, there is currently no means to determine seismic anisotropy of single lithologies (at the scale of hundreds of meters) at the scale of investigation (several kilometers), and thus the estimates presented above are useful only for bulk V_P. Finally, up to 10 km depth at which porosity could have an appreciable influence on V_P and ρ (Behn & Kelemen, 2003), microcracks that contribute to the rock porosity are mostly closed and any porosity effect on V_P and ρ is negligible as tested experimentally at ∼0.5 GPa (Burlini & Fountain, 1993; A. S. Zappone, 1994). Also, the near-absence of active tectonics/seismicity in this portion of the Alps where the IVZ is located (The ECORS-CROP Deep Seismic Sounding Group, 1989; A. Zappone et al., 1992) does not favor high porosities at shallow depth as observed in previous continental drilling projects (e.g., Veselov et al., 1987).

The three-dimensional single-interface crustal density model of Scarponi et al. (2020) defines the shape of the IGB using a compilation of published gravity data and 207 new relative gravity measurements (approaching an optimal spatial coverage of 1 data point per 4–9 km^2 across the IVZ), tectonic maps, and rock laboratory analyses of densities together with a mineral properties database. This data compilation produces a novel surface rock-density map of the IVZ that is taken into account for Bouguer plate and terrain corrections. The final density model, with an optimal fit to the observations, displays acceptable densities of 3,000–3,400 kg/m^3 based on 2,700–2,900 kg/m^3 background density and 300–500 kg/m^3 anomaly. This model is the currently best available one for the Valsesia and for the IVZ in general. We finally compare the outcomes of the thermodynamic calculations with the models of Diehl et al. (2009) for V_P and Scarponi et al. (2020) for ρ (Figure 5).

3. Results

We present four sets of V_P- and ρ-depth profiles based on four scenarios: (I) laboratory constraints, as well as thermodynamic calculations using (II) anhydrous ultramafic rocks (peridotite and pyroxenite), (III) anhydrous gabbro, and (IV) peridotite and gabbro with $H_2O \leq 1$ wt.%, based on their amphibole content (Figure 5). We report only those rock types that display the end-member V_P and ρ profiles with depth to assess the composition of the IGB.

The profile of scenario I (indicated by solid and dashed black lines in Figure 5) was obtained by using the relationships between V_P and the volumetric proportion of serpentine in ultramafic rocks reported in the IGB model depicted by Zhao et al. (2015): 60 vol.% serpentine in the depth range from 3 to 30 km and 30 vol.% serpentine at > 30 km, respectively (Figure 5). At the depth of 3 km (Figure 5b), calculated V_P of gabbros are generally faster by ∼0.7 km/s than the large-scale tomographic V_P constraint of Diehl et al. (2009) and the calculated serpentinized harzburgite (Zhao et al., 2015), but slower than pyroxenite and lherzolite by 0.5 km/s and 1.5 km/s, respectively. At >3 km depth, the V_P data of the serpentinized harzburgite underestimate and therefore do not match with the geophysical constraints of Diehl et al. (2009) in the entire lithospheric column (3–50 km depth). The ρ of the serpentinized harzburgite varies from 3,000 to 3,200 kg/m^3 (Zhao et al., 2015) and fits the lowest density-difference model of Scarponi et al. (2020) (Figure 5c).

V_P and ρ profiles in scenario II (indicated by dark green field in Figure 5) refer to anhydrous pyroxenite, lherzolite, dunite, and harzburgite of the IVZ. At 3 km depth, calculated V_P ranges from 7.6 (pyroxenite) to 8.2 km/s (dunite) and is higher than the V_P estimated by the model of Diehl et al. (2009) by ∼1.5 km/s (Figure 5b) in the depth range 3–30 km. Calculated ρ of 3,250 (dunite) to 3,350 kg/m3 (pyroxenite) fits with the upper Δρ range of the model of Scarponi et al. (2020) (Figure 5c). The minor increase in both V_P and ρ (∼2%) observed at ∼10 and ∼40 km depths correspond to the calculated paleo-pressures of plagioclase-spinel and spinel-garnet transition in peridotite, respectively (Table 2).
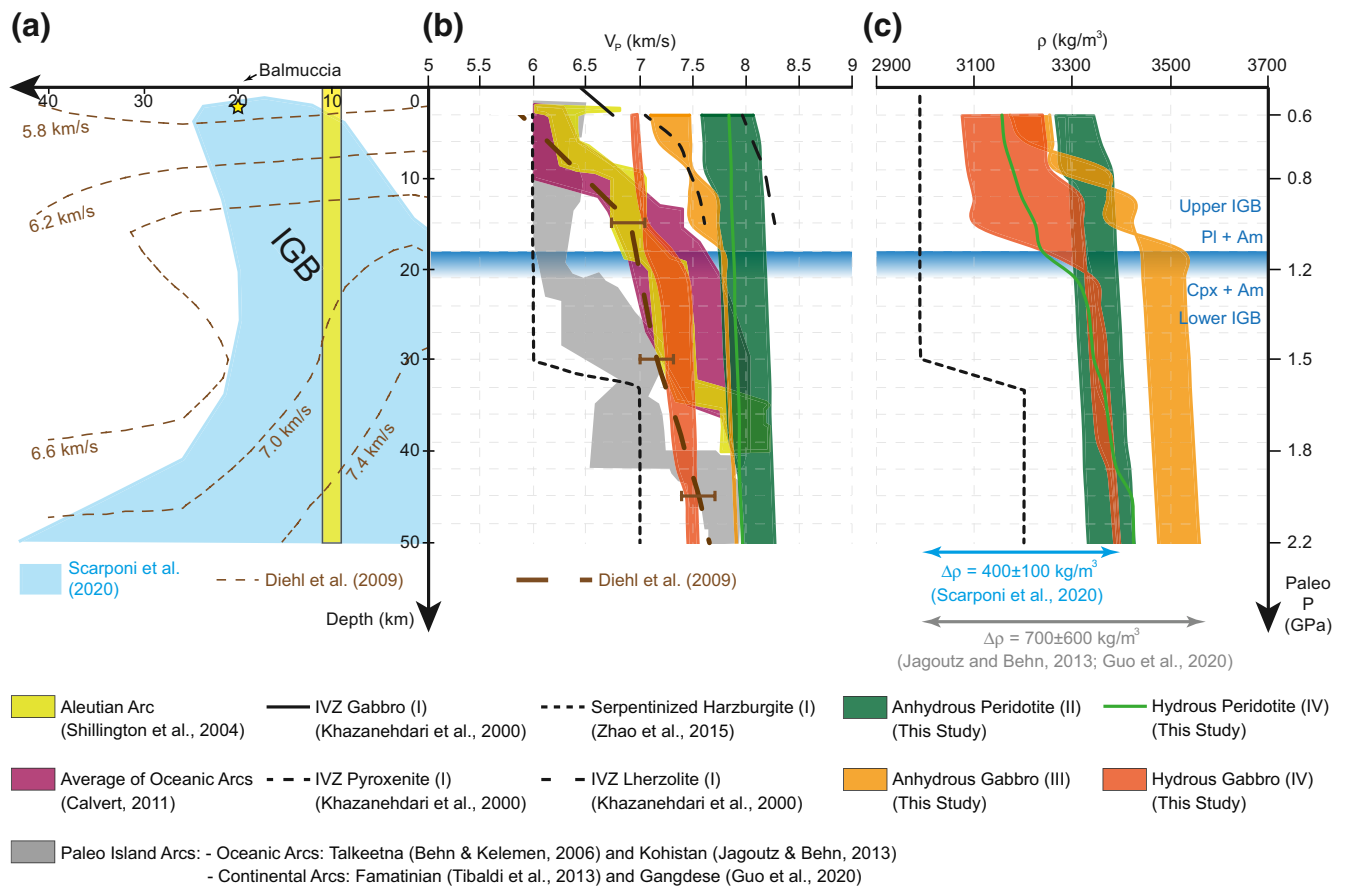
Figure 5. Seismic compressional wave velocity (V_P) (b) and rock density (ρ) (c) profiles along a depth-structure profile (yellow) beneath Valsesia (a). Data are based on: (I) laboratory constraints for gabbro (0–3 km), serpentinized harzburgite, pyroxenite, and lherzolite (3–15 km), and thermodynamic calculations for (II) anhydrous ultramafic rocks, (III) anhydrous gabbros, and (IV) hydrous lherzolite and gabbros of the IVZ (3–50 km). V_P data of the Aleutian arc (Shillington et al., 2004), average of oceanic arcs (Calvert, 2011), and oceanic and continental paleo-arc systems (Behn & Kelemen, 2006; Guo et al., 2020; Jagoutz & Behn, 2013; Tibaldi et al., 2013) are also reported. Brown bars indicate values as uncertainties in V_P model grid points (every 15 km of depth) of Diehl et al. (2009). Light blue arrow indicates ρ variation range (Δρ) expected from gravimetric measurements (Scarponi et al., 2020); gray bar indicates Δρ for continental Kohistan (Jagoutz & Behn, 2013) and Gangdese (Guo et al., 2020) paleo-arcs from mineral density calculated using pressures derived from geothermobarometry of the observed mineral compositions and temperature calculated along steady-state 60 mW/m^2 geotherm. The blue gradient area divides upper (amphibole gabbro = plagioclase [Pl] + amphibole [Am]) from lower IGB (pyroxene hornblendite = clinopyroxene [Cpx] + amphibole [Am]). The V_P increase is not linearly correlated with ρ increase. IGB, Ivrea Geophysical Body; IVZ, Ivrea-Verbano Zone.

V_P and ρ profiles of anhydrous gabbroic rocks of the IVZ are summarized in scenario III (indicated by light orange field in Figure 5). With the concomitant modal increase of clinopyroxene (from 30 to 68 vol.%) and orthopyroxene (from 5 to 19 vol.%) and decrease of plagioclase (from 35 to 0 vol.%) in the depth range of 3–18 km within the IGB, both gabbroic compositions display a gradual increase of V_P and ρ of ~5% and ~10%, respectively (Figure 5; Table 2). Beneath 18 km depth, the original gabbros become websterites characterized by both V_P and ρ increasing linearly with no appreciable changes in the gradient (Figure 5). The V_P of anhydrous gabbroic rocks tend to be larger than the V_P constraint of Diehl et al. (2009) by ~1.0 km/s at 3 km depth and by ~0.5 km/s up to 50 km depth (Figure 5b). The ρ of anhydrous gabbroic rocks only fits the upper Δρ range of the model of Scarponi et al. (2020) up to 10 km depth (Figure 5c).

Scenario IV (indicated by solid light green line and dark orange field in Figure 5) summarizes V_P and ρ profiles of amphibole gabbro (<18 km depth)/pyroxene hornblendite (>18 km depth) and hydrous lherzolite of the IVZ. While the lherzolite is characterized by almost constant V_P with depth (7.8 km/s) and limited increase of ρ (maximum ~2% in the depth range 9–15 km), the gabbro displays a marked increase of V_P (from 6.9 km/s at 3 km depth to 7.2–7.5 km/s at 30 km depth) and ρ (from 3,140 to 3,320 kg/m^3; Figure 5). Abundant plagioclase significantly lowers both V_P and ρ to 6.8–7.0 km/s and 3,250 kg/m^3 in the upper

Table 2
Summary of V_P and ρ from the Thermodynamic Calculations Based on Representative Rock Compositions listed in Table 1

Rock type	Phase/rock stability	Depth (km)	P (GPa)	V_P (km/s)	ρ (kg/ m³)
	Anhydrous ultramafic rocks of the IVZ				
Balmuccia lherzolite average	Pl-Lherzolite	3	0.60	7.80	3,245
	Pl-Lherzolite	6	0.70	7.82	3,251
	Pl-Lherzolite	9	0.79	7.83	3,256
	Spl-Lherzolite	12	0.89	7.93	3,305
	Spl-Lherzolite	15	0.98	7.94	3,308
	Spl-Lherzolite	18	1.10	7.95	3,311
	Spl-Lherzolite	21	1.20	7.96	3,312
	Spl-Lherzolite	24	1.29	7.97	3,317
	Spl-Lherzolite	27	1.39	7.98	3,320
	Spl-Lherzolite	30	1.48	7.99	3,322
	Spl-Lherzolite	33	1.58	8.00	3,325
	Spl + Grt-Lherzolite	36	1.67	8.07	3,344
	Grt-Lherzolite	39	1.77	8.10	3,352
	Grt-Lherzolite	42	1.86	8.11	3,355
	Grt-Lherzolite	45	1.96	8.12	3,358
	Grt-Lherzolite	48	2.06	8.13	3,361
	Grt-Lherzolite	51	2.15	8.15	3,364
	Grt-Lherzolite	54	2.25	8.16	3,367
	Grt-Lherzolite	57	2.34	8.17	3,370
	Grt-Lherzolite	60	2.44	8.18	3,373
Balmuccia diopside pyroxenite average	Cr-Di Pyroxenite	3	0.60	7.54	3,222
	Cr-Di Pyroxenite	6	0.69	7.56	3,228
	Cr-Di Pyroxenite	9	0.79	7.57	3,235
	Spl-Pyroxenite	12	0.88	7.68	3,294
	Spl-Pyroxenite	15	0.98	7.69	3,297
	Spl-Pyroxenite	18	1.07	7.70	3,301
	Spl-Pyroxenite	21	1.17	7.72	3,304
	Spl-Pyroxenite	24	1.26	7.73	3,307
	Spl-Pyroxenite	27	1.36	7.74	3,310
	Spl-Pyroxenite	30	1.45	7.75	3,313
	Spl-Pyroxenite	33	1.55	7.77	3,316
	Spl-Pyroxenite	36	1.64	7.78	3,320
	Spl + Grt-Pyroxenite	39	1.74	7.80	3,326
	Spl + Grt-Pyroxenite	42	1.83	7.87	3,345
	Grt-Pyroxenite	45	1.93	7.89	3,351
	Grt-Pyroxenite	48	2.02	7.91	3,355
	Grt-Pyroxenite	51	2.12	7.92	3,359
	Grt-Pyroxenite	54	2.21	7.94	3,362
	Grt-Pyroxenite	57	2.31	7.95	3,366
	Grt-Pyroxenite	60	2.40	7.96	3,369

Table 2
Continued

Rock type	Phase/rock stability	Depth (km)	P (GPa)	V_P (km/s)	ρ (kg/m^3)
Balmuccia dunite average	Pl-Dunite	3	0.60	8.00	3,273
	Pl-Dunite	6	0.70	8.06	3,289
	Pl-Dunite	9	0.79	8.07	3,292
	Grt-Dunite	12	0.89	8.09	3,301
	Grt-Dunite	15	0.99	8.10	3,304
	Grt-Dunite	18	1.09	8.11	3,307
	Grt-Dunite	21	1.18	8.12	3,310
	Grt-Dunite	24	1.28	8.13	3,313
	Grt-Dunite	27	1.38	8.14	3,316
	Grt-Dunite	30	1.47	8.15	3,319
	Grt-Dunite	33	1.57	8.16	3,321
	Grt-Dunite	36	1.67	8.16	3,324
	Grt-Dunite	39	1.77	8.17	3,327
	Grt-Dunite	42	1.86	8.18	3,330
	Grt-Dunite	45	1.96	8.19	3,332
	Grt-Dunite	48	2.06	8.20	3,335
	Grt-Dunite	51	2.15	8.21	3,338
	Grt-Dunite	54	2.25	8.22	3,341
	Grt-Dunite	57	2.35	8.23	3,343
	Grt-Dunite	60	2.45	8.23	3,346
Finero peridotite average	Pl-Harzburgite	3	0.60	7.95	3,257
	Pl + Spl-Harzburgite	6	0.70	7.99	3,267
	Pl + Spl-Harzburgite	9	0.79	8.00	3,271
	Spl-Harzburgite	12	0.89	8.04	3,292
	Spl-Harzburgite	15	0.98	8.05	3,295
	Spl-Harzburgite	18	1.08	8.06	3,297
	Spl-Harzburgite	21	1.18	8.07	3,300
	Spl-Harzburgite	24	1.27	8.08	3,302
	Spl-Harzburgite	27	1.37	8.09	3,305
	Spl-Harzburgite	30	1.46	8.10	3,307
	Spl-Harzburgite	33	1.56	8.10	3,310
	Spl-Harzburgite	36	1.65	8.11	3,313
	Grt-Harzburgite	39	1.75	8.15	3,323
	Grt-Harzburgite	42	1.85	8.16	3,326
	Grt-Harzburgite	45	1.94	8.17	3,329
	Grt-Harzburgite	48	2.04	8.18	3,331
	Grt-Harzburgite	51	2.13	8.19	3,334
	Grt-Harzburgite	54	2.23	8.20	3,337
	Grt-Harzburgite	57	2.33	8.21	3,339
	Grt-Harzburgite	60	2.42	8.21	3,342

Table 2
Continued

Rock type	Phase/rock stability	Depth (km)	P (GPa)	V_P (km/s)	ρ (kg/m^3)
Balmuccia lherzolite FE37	Pl-Lherzolite	3	0.60	7.88	3,307
	Pl-Lherzolite	6	0.70	7.89	3,311
	Pl-Lherzolite	9	0.79	7.91	3,315
	Spl-Lherzolite	12	0.89	7.92	3,322
	Spl-Lherzolite	15	0.99	7.93	3,325
	Spl-Lherzolite	18	1.09	7.94	3,328
	Spl-Lherzolite	21	1.18	7.95	3,331
	Spl-Lherzolite	24	1.28	7.96	3,334
	Spl-Lherzolite	27	1.38	7.97	3,337
	Spl-Lherzolite	30	1.48	7.98	3,340
	Spl-Lherzolite	33	1.57	7.99	3,342
	Spl-Lherzolite	36	1.67	8.00	3,345
	Grt-Lherzolite	39	1.77	8.02	3,350
	Grt-Lherzolite	42	1.87	8.03	3,353
	Grt-Lherzolite	45	1.96	8.04	3,356
	Grt-Lherzolite	48	2.06	8.05	3,359
	Grt-Lherzolite	51	2.16	8.06	3,362
	Grt-Lherzolite	54	2.25	8.07	3,365
	Grt-Lherzolite	57	2.35	8.08	3,368
	Grt-Lherzolite	60	2.45	8.09	3,371
Balmuccia pyroxenite IV35	Pl-Pyroxenite	3	0.60	7.60	3,258
	Pl + Sp-Pyroxenite	6	0.70	7.64	3,274
	Pl-Pyroxenite	9	0.79	7.81	3,370
	Spl-Pyroxenite	12	0.89	7.82	3,373
	Spl-Pyroxenite	15	0.98	7.83	3,376
	Spl-Pyroxenite	18	1.08	7.85	3,379
	Spl-Pyroxenite	21	1.18	7.86	3,382
	Spl-Pyroxenite	24	1.27	7.87	3,385
	Spl-Pyroxenite	27	1.37	7.88	3,388
	Spl-Pyroxenite	30	1.46	7.89	3,390
	Spl-Pyroxenite	33	1.56	7.90	3,393
	Spl-Pyroxenite	36	1.65	7.91	3,396
	Spl-Pyroxenite	39	1.75	7.92	3,399
	Spl-Pyroxenite	42	1.85	7.93	3,402
	Spl-Pyroxenite	45	1.94	7.94	3,405
	Spl + Grt-Pyroxenite	48	2.04	8.07	3,442
	Grt-Pyroxenite	51	2.13	8.10	3,450
	Grt-Pyroxenite	54	2.23	8.11	3,453
	Grt-Pyroxenite	57	2.33	8.12	3,456
	Grt-Pyroxenite	60	2.42	8.13	3,459

Table 2
Continued

Rock type	Phase/rock stability	Depth (km)	P (GPa)	V_P (km/s)	ρ (kg/m^3)
Finero harzburgite average	Pl + Spl-Harzburgite	3	0.60	7.93	3,320
	Pl + Spl-Harzburgite	6	0.70	7.97	3,333
	Spl-Harzburgite	9	0.80	8.01	3,353
	Spl-Harzburgite	12	0.89	8.02	3,356
	Spl-Harzburgite	15	0.99	8.03	3,359
	Spl-Harzburgite	18	1.09	8.04	3,361
	Spl-Harzburgite	21	1.19	8.05	3,364
	Spl-Harzburgite	24	1.28	8.05	3,367
	Spl-Harzburgite	27	1.38	8.06	3,370
	Spl-Harzburgite	30	1.48	8.07	3,372
	Spl-Harzburgite	33	1.58	8.08	3,375
	Spl-Harzburgite	36	1.67	8.09	3,378
	Spl-Harzburgite	39	1.77	8.10	3,380
	Grt-Harzburgite	42	1.87	8.12	3,387
	Grt-Harzburgite	45	1.97	8.13	3,390
	Grt-Harzburgite	48	2.07	8.14	3,393
	Grt-Harzburgite	51	2.16	8.15	3,396
	Grt-Harzburgite	54	2.26	8.16	3,399
	Grt-Harzburgite	57	2.36	8.17	3,402
	Grt-Harzburgite	60	2.46	8.18	3,405
Mafic anhydrous rocks and mafic and ultramafic hydrous rocks of the IVZ					
Lower mafic complex olivine gabbro IV117	Spl-Gabbro	3	0.60	7.42	3,236
	Spl-Gabbro	6	0.70	7.43	3,242
	Spl-Gabbro	9	0.79	7.45	3,247
	Spl+2Px-Gabbro	12	0.89	7.67	3,391
	Spl+2Px-Gabbro	15	0.98	7.68	3,395
	Spl+2Px + Ky-Gabbro	18	1.08	7.72	3,412
	Spl+2Px + Ky-Gabbro	21	1.17	7.73	3,415
	Spl+2Px + Ky-Gabbro	24	1.27	7.75	3,419
	Spl+2Px + Ky-Gabbro	27	1.36	7.76	3,422
	Spl+2Px + Ky-Gabbro	30	1.46	7.77	3,425
	Spl+2Px + Ky-Gabbro	33	1.55	7.78	3,428
	Spl+2Px + Ky-Gabbro	36	1.65	7.79	3,431
	Spl+2Px + Ky-Gabbro	39	1.74	7.80	3,434
	Spl+2Px + Ky-Gabbro	42	1.84	7.82	3,437
	Spl+2Px + Ky-Gabbro	45	1.93	7.83	3,440
	Spl+2Px + Ky-Gabbro	48	2.03	7.84	3,443
	Spl+2Px + Ky-Gabbro	51	2.12	7.85	3,446
	Spl+2Px + Ky-Gabbro	54	2.22	7.86	3,449
	Spl+2Px + Ky-Gabbro	57	2.31	7.87	3,452
	Spl+2Px + Ky-Gabbro	60	2.41	7.88	3,455

Table 2
Continued

Rock type	Phase/rock stability	Depth (km)	P (GPa)	V_P (km/s)	ρ (kg/m^3)
Finero gabbro average	Gabbro	3	0.60	7.05	3,156
	Gabbro	6	0.69	7.13	3,189
	Spl-Gabbro	9	0.79	7.40	3,339
	Spl-Gabbro	12	0.88	7.41	3,344
	Spl-Gabbro	15	0.97	7.43	3,349
	Spl + Ky-Gabbro	18	1.06	7.72	3,488
	Spl + Ky-Gabbro	21	1.16	7.74	3,492
	Spl + Ky-Gabbro	24	1.25	7.75	3,494
	Spl + Ky-Gabbro	27	1.34	7.76	3,497
	Spl + Ky-Gabbro	30	1.44	7.77	3,501
	Spl + Ky-Gabbro	33	1.53	7.78	3,503
	Spl + Ky-Gabbro	36	1.62	7.79	3,506
	Spl + Ky-Gabbro	39	1.71	7.80	3,509
	Spl + Ky-Gabbro	42	1.81	7.82	3,512
	Spl + Ky-Gabbro	45	1.90	7.83	3,515
	Spl + Ky-Gabbro	48	1.99	7.84	3,518
	Spl + Ky-Gabbro	51	2.09	7.85	3,522
	Eclogite	54	2.18	7.87	3,529
	Eclogite	57	2.27	7.88	3,532
	Eclogite	60	2.36	7.90	3,535
Finero gabbro with 1 wt% H_2O	Am-Gabbro	3	0.60	6.88	3,140
	Am-Gabbro	6	0.69	6.89	3,145
	Am-Gabbro	9	0.78	6.91	3,161
	Am-Gabbro	12	0.88	6.94	3,178
	Am-Gabbro	15	0.97	6.99	3,204
	Am-Gabbro	18	1.06	7.01	3,218
	Py-Hornblendite	21	1.15	7.11	3,282
	Py-Hornblendite	24	1.25	7.16	3,305
	Py-Hornblendite	27	1.34	7.18	3,312
	Py-Hornblendite	30	1.43	7.20	3,318
	Py-Hornblendite	33	1.52	7.21	3,336
	Py-Hornblendite	36	1.62	7.24	3,344
	Py-Hornblendite	39	1.71	7.26	3,351
	Py-Hornblendite	42	1.80	7.30	3,362
	Py-Hornblendite	45	1.89	7.38	3,390
	Py-Hornblendite	48	1.99	7.39	3,394
	Py-Hornblendite	51	2.08	7.40	3,397
	Py-Hornblendite	54	2.17	7.43	3,427
	Py-Hornblendite	57	2.26	7.44	3,433
	Py-Hornblendite	60	2.36	7.45	3,437

Table 2
Continued

Rock type	Phase/rock stability	Depth (km)	P (GPa)	V_P (km/s)	ρ (kg/m^3)
Finero gabbro with 0.1 wt% H_2O	Gabbro	3	0.60	7.04	3,166
	Gabbro	6	0.69	7.08	3,186
	Spl-Gabbro	9	0.79	7.17	3,233
	Spl-Gabbro	12	0.88	7.25	3,278
	Spl-Gabbro	15	0.97	7.31	3,308
	Spl + Ky-Gabbro	18	1.07	7.41	3,350
	Spl + Ky-Gabbro	21	1.16	7.46	3,370
	Grt + Ky-Gabbro	24	1.25	7.67	3,459
	Grt + Ky-Gabbro	27	1.35	7.74	3,488
	Grt + Ky-Gabbro	30	1.44	7.74	3,491
	Grt + Ky-Gabbro	33	1.53	7.75	3,494
	Grt + Ky-Gabbro	36	1.62	7.76	3,497
	Grt + Ky-Gabbro	39	1.72	7.77	3,500
	Grt + Ky-Gabbro	42	1.81	7.78	3,503
	Grt + Ky-Gabbro	45	1.90	7.79	3,506
	Eclogite	48	2.00	7.80	3,509
	Eclogite	51	2.09	7.81	3,512
	Eclogite	54	2.18	7.82	3,515
	Eclogite	57	2.28	7.84	3,519
	Eclogite	60	2.37	7.85	3,522
Sessera gabbro with 1 wt% H_2O	Am-Gabbro	3	0.60	6.92	3,061
	Am-Gabbro	6	0.69	6.94	3,066
	Am-Gabbro	9	0.78	6.96	3,072
	Am-Gabbro	12	0.87	6.99	3,084
	Am-Gabbro	15	0.96	7.02	3,089
	Am-Gabbro	18	1.05	7.25	3,227
	Py-Hornblendite	21	1.14	7.40	3,319
	Py-Hornblendite	24	1.23	7.43	3,328
	Py-Hornblendite	27	1.32	7.43	3,338
	Py-Hornblendite	30	1.41	7.44	3,342
	Py-Hornblendite	33	1.50	7.45	3,345
	Py-Hornblendite	36	1.59	7.46	3,349
	Py-Hornblendite	39	1.68	7.47	3,353
	Py-Hornblendite	42	1.77	7.47	3,357
	Py-Hornblendite	45	1.86	7.48	3,361
	Py-Hornblendite	48	1.95	7.49	3,364
	Py-Hornblendite	51	2.04	7.50	3,369
	Py-Hornblendite	54	2.13	7.52	3,381
	Py-Hornblendite	57	2.22	7.53	3,396
	Py-Hornblendite	60	2.31	7.55	3,411

Table 2
Continued

Rock type	Phase/rock stability	Depth (km)	P (GPa)	V_P (km/s)	ρ (kg/m^3)
Finero harzburgite with 1 wt% H$_2$O	Am + Phl-Harzburgite	3	0.60	7.78	3,266
	Am + Phl-Harzburgite	6	0.70	7.79	3,268
	Am + Phl-Wehrlite	9	0.79	7.80	3,271
	Am + Phl-Wehrlite	12	0.89	7.80	3,274
	Am + Phl-Wehrlite	15	0.98	7.81	3,276
	Am + Phl-Wehrlite	18	1.08	7.82	3,279
	Am + Phl-Wehrlite	21	1.18	7.83	3,282
	Am + Phl-Wehrlite	24	1.27	7.83	3,285
	Am + Phl-Wehrlite	27	1.37	7.84	3,287
	Am + Phl-Wehrlite	30	1.47	7.85	3,290
	Am + Phl-Wehrlite	33	1.56	7.86	3,293
	Am + Phl-Wehrlite	36	1.66	7.87	3,296
	Am + Phl-Wehrlite	39	1.75	7.87	3,298
	Am + Phl-Wehrlite	42	1.85	7.87	3,299
	Am + Phl-Wehrlite	45	1.95	7.88	3,302
	Am + Phl-Wehrlite	48	2.04	7.89	3,304
	Am + Phl-Wehrlite	51	2.14	7.90	3,307
	Am + Phl-Wehrlite	54	2.23	7.90	3,310
	Am + Phl-Wehrlite	57	2.33	7.91	3,313
	Am + Phl-Wehrlite	60	2.43	7.92	3,316

Abbreviations: Am, amphibole; Cr-Di, Cr-diopisde; Grt, garnet; IVZ, Ivrea-Verbano Zone; Ky, kyanite; Phl, phlogopite; Pl, plagioclase; Px, pyroxene; Spl, spinel.

IGB (3–21 km depth; Figure 6). In the lower IGB where gabbros become pyroxene hornblendites (and kyanite-bearing eclogites; Figure 6a; Godovikov & Kennedy, 1968) with the disappearance of plagioclase (21–50 km depth), abundant clinopyroxene (up to ~33 vol.%; Figure 6) favors V_P and ρ increase (Figure 5). The V_P of hydrous lherzolite and amphibole gabbro/pyroxene hornblendite differ by ~1 km/s between each other (Figure 5b). While the V_P of hydrous lherzolite is higher than the V_P constraint of Diehl et al. (2009) by ~1 km/s at < 30 km depth and ~0.5 km/s at > 30 km depth, respectively, the V_P of amphibole gabbro/pyroxene hornblendite fits the V_P constraint of Diehl et al. (2009) throughout the whole lithospheric column up to 50 km depth (Figure 5b). The ρ of both hydrous lherzolite and amphibole gabbro/pyroxene hornblendite fits the upper $\Delta\rho$ range of the model of Scarponi et al. (2020) between 20 and 50 km depth, whereas at < 20 km depth amphibole gabbro ranges from 3,000 to 3,200 kg/m^3 (Figure 5c).

In the amphibole gabbro/pyroxene hornblendite, the modal content of amphibole remains broadly constant (between ~45 and ~50 vol.%) and variations of modal amphibole appear to be inversely correlated to the variations of modal orthopyroxene after the disappearance of plagioclase at 18–20 km depth (Figure 6). The two amphibole gabbros considered in this study (Finero gabbro in Figure 6a and Sessera gabbro in Figure 6b) show discrepancies in initial modal proportions of amphibole, clinopyroxene, and plagioclase. Above all, in the plagioclase-free pyroxene hornblendite, the slightly different modal amounts of garnet forming from 10 to 12 km depth and orthopyroxene from 18 km depth affect the calculated V_P increase with depth. Indeed, V_P of Finero gabbro–pyroxene hornblendite increases linearly by 0.1 km/s every 10 km depth with 1 vol.% garnet and <5 vol.% orthopyroxene (Figure 6a), whereas V_P of Sessera gabbro increases sharply by 0.4 km/s at ~20 km and, beneath this depth, the Sessera pyroxene hornblendite is characterized by a slight increase of V_P (7.5 km/s) down to 50 km depth in presence of 2 vol.% garnet and <10 vol.% orthopyroxene (Figure 6b).
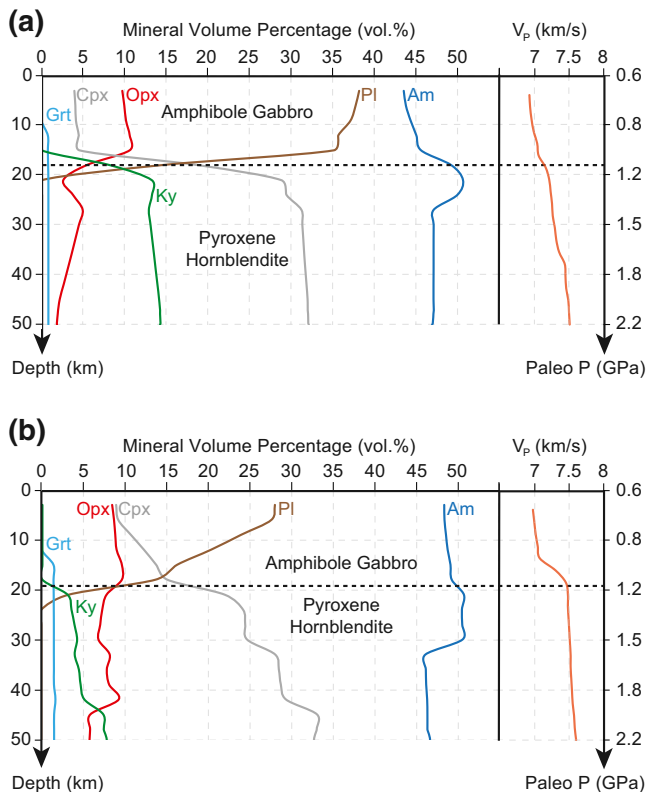
Figure 6. Mineral modal proportions of the hydrous gabbros from Finero Mafic Complex (a) and Val Sessera (b), based on the thermodynamic calculations of Scenario IV. Original amphibole gabbros transition to pyroxene hornblendite after the disappearance of plagioclase at 18–20 km depth (corresponding to a paleo pressure of 1.0–1.2 GPa). Accessory (<5 vol.%) and minor mineral phases (<10 vol.%), such as quartz, olivine, ilmenite, sanidine, phlogopite, and staurolite, are not reported. The black dashed line reporting the divide between amphibole gabbro and pyroxene hornblendite is set at plagioclase <5 vol.%. Mineral abbreviations: Am, amphibole; Cpx, clinopyroxene; Grt, garnet; Ky, kyanite; Opx, orthopyroxene; Pl, plagioclase.

Overall, both anhydrous and hydrous ultramafic rocks overestimate the high V_P at the shallowest point of the discontinuity modeled by Scarponi et al. (2020). Conversely, the gabbroic compositions appear to meet the geophysical constraints of the shallow interface for both V_P and ρ, considering that the gravity anomalies constrain a relative density change at depth (Figure 5). All rock types from Scenarios II–IV variably overestimate V_P with respect to the tomography-derived constraints of Diehl et al. (2009) and the calculated V_P of paleo-island arcs (Figure 5). However, the amphibole gabbro-pyroxene hornblendite is the one that most closely approach the tomography-derived constraints and also appears to be consistent with the V_P of oceanic arc crust in the depth range of 10–35 km (Figure 5).

4. Discussion

This study provides compositional bounds on one of the largest geophysical anomalies generated by a shallow volume of dense rocks originally representing the lower continental crust and upper mantle. Amphibole gabbros (<21 km depth; Figure 6) and pyroxene hornblendite/kyanite-bearing eclogites (>18 km depth; Figure 6) match most closely the geophysical constraints on the IGB (Figure 5). Especially, after the disappearance of plagioclase at >18 km depth, V_P exceeds 7 km/s owing to the increase of modal clinopyroxene (Figure 6), with the increase of the high-pressure jadeite component dissolved in clinopyroxene solid solution due to the albite-out reaction (albite = jadeite + quartz reaction at 1.6–1.8 GPa at 600°C–700°C; Holland, 1980) and with the appearance of limited modal garnet (<3 vol.%; Figure 6). Because of the high seismic velocities of jadeite (V_P > 8.6 km/s) and garnet (V_P > 8.5 km/s), even small amounts of these components may significantly influence the V_P of a bulk rock (Babuska et al., 1978; Behn & Kelemen, 2003; Sobolev & Babeyko, 1994). In this study, garnet and jadeitic clinopyroxene in pyroxene hornblendite favor the increase of V_P by 0.5 km/s from the original V_P of amphibole gabbros (7 km/s; Figure 6). Neither anhydrous nor partially hydrated ultramafic rocks are consistent with the available geophysical constraints for the IGB (Figure 5). The IGB is therefore likely characterized by a thick pile of hydrous rocks ranging from amphibole gabbros to pyroxene hornblendites/kyanite-bearing eclogites. We note that the three-dimensional model of Scarponi et al. (2020) permits to exclude highly dense rock types (pyroxenite, peridotite, and eclogite); however, ρ-depth profiles alone do not resolve the compositional ambiguity of the IGB.

V_P-ρ correlations using the Nafe-Drake-Birch-Woollard plot (Birch, 1960, 1961; Nafe & Drake, 1957; Woollard, 1975) help estimate rock densities for gravity modeling from seismic refraction velocities and, conversely, facilitate the use of rock densities to constrain plausible seismic velocities (Figure 7). If we compare these V_P-ρ relations with geophysical and laboratory data, there is a general discrepancy that consistently points to higher values for the modeled data. The modeled rock types are based on both IGB and the surroundings having the same vertical ρ gradient, similar to the increase proposed atop the IGB by Berckhemer (1969), Kissling (1984), Bürki et al., (1990), and Scarponi et al. (2020) (Figure 7). The latest gravity model of Scarponi et al. (2020) suggest that the relative ρ difference (400 kg/m³) should be used as a constraint between the IGB and the surroundings, beyond a likely vertical density gradient. In conclusion, amphibole gabbros-pyroxene hornblendite best fit the current geophysical observations of the IGB (Figure 7) in terms of relatively low V_P (7–7.5 km/s) and high ρ (3,100–3,300 kg/m³) in the depth range 3–50 km (Figures 3–5).
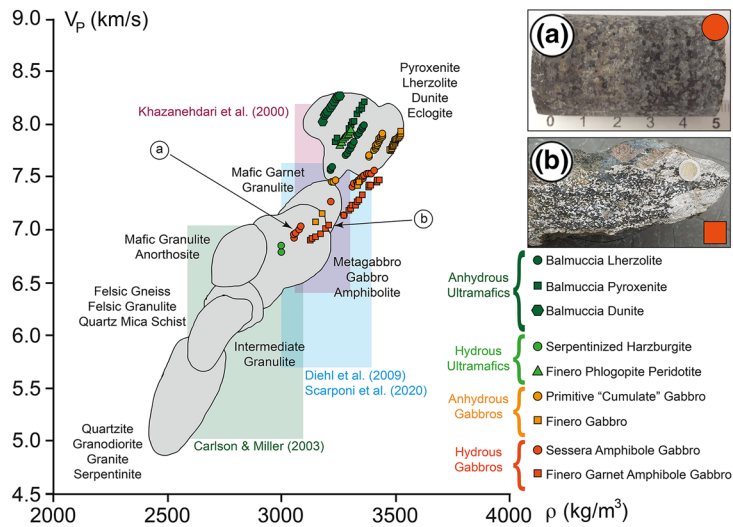
Figure 7. Nafe-Drake-Birch-Woolard plot with the modeled data of Figure 5 and with literature data of V_P and ρ of different rock types at a depth of 20 km and a temperature of 300°C ± 15°C (corresponding to an average continental geotherm; Christensen & Mooney, 1995), indicated by gray fields. Light colored rectangles indicate laboratory data of serpentinized harzburgite (green; Miller & Christensen, 1997) and IVZ rocks, including schists, granites, amphibolites, mafic granulites, and ultramafic rocks (purple; Khazanehdari et al., 2000), as referenced, and models of Diehl et al. (2009) for V_P and Scarponi et al. (2020) for ρ (light blue). Image insets display the IVZ amphibole gabbros with abundant plagioclase (a) and garnet (b) that best match the geophysical signature of the IGB. IGB, Ivrea Geophysical Body; IVZ, Ivrea-Verbano Zone.

The IGB showcases V_P consistent with relatively high-density rocks (Scarponi et al., 2020) and V_P higher than those reported for exposed crustal sections in published compilations (Behn & Kelemen, 2003; Rudnick and Fountain, 1995, and references therein) by 0.4–0.8 km/s (Figure 8). The V_P associated to the rocks identified in the field (amphibole gabbro) and predicted using thermodynamic calculations (pyroxene hornblendite) indicate that the V_P increase is not only dependent on changes in pressures that favor the stability of high-V_P minerals (garnet and clinopyroxene with high modal jadeite component), but also on the transition toward more mafic/ultramafic cumulate rock compositions, such as the pyroxene hornblendite from this study (Figure 6). The overall crustal thickness of the IVZ (∼30 km) combined with the upper IGB characterized by dominant plagioclase (∼18 km; Figures 5 and 6) exceeds the thicknesses of the exposed crustal sections observed worldwide (Figure 1) and the crustal thicknesses assessed based on compilations
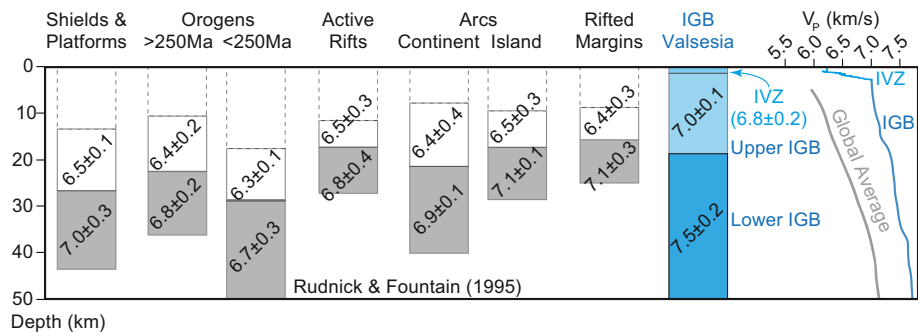

Figure 8. Crustal V_P sections for a number of continental environments based on the compilation of Rudnick and Fountain (1995), supplemented by studies on arcs and rifted margins summarized by Behn and Kelemen (2003), compared to this study on the present-day IGB (highlighted in blue color) and the average/global crustal V_P model of Christensen and Mooney (1995). White boxes indicate upper/middle crust and gray boxes refer to lower crust. Variability represents the standard deviation of values from all studies in each crustal section and is similar to the uncertainty in V_P estimates for the lower crust in each study. Dashed squares indicate crustal sections characterized by $V_P \leq 6.2$ km/s. IGB, Ivrea Geophysical Body; IVZ, Ivrea-Verbano Zone.

of geophysical, petrological, and geochemical data (Figure 8). The IVZ + upper IGB section appears to be comparable to the Kohistan paleo-island arc section (without the volcanics in Figure 1). The IVZ + upper IGB section could possibly be a complete record of the continental crust produced in the early Permian above the cumulate body of pyroxene hornblendite composing the lower portion of the IGB (Figure 6).

5. Implications

Estimates of the composition of Earth's continental crust are highly variable (49–65 wt.% SiO_2; Hacker et al., 2015; Rudnick & Gao, 2003), with no consensus about the composition of the lower crust, as it is often difficult to distinguish based on seismic wave velocities, geochemical compositions, and heat flow constraints (Hacker et al., 2015). Analysis of global or regional datasets cannot readily disentangle the relevant processes that control the composition of the crust and, in particular, the lower crust. Therefore, studying one of best known crustal sections in the world—the IVZ—provides new insights as it is unique by exposing an almost complete section of crustal rocks of ~30 km. The IVZ has been investigated by the scientific community over the last 50 years and is a reference case for many models of the lower continental crust (e.g., Salisbury & Fountain, 1990). In the light of our results, the lower crustal section of the IVZ + upper IGB and the cumulate portion of the lower IGB that satisfy the present-day geophysical constraints in terms of V_P (7–7.5 km/s) and ρ (3,100–3,300 kg/m^3) seem more mafic (~45 wt.% SiO_2) than the proposed estimates of bulk rock composition of the lower crust (49–65 wt.% SiO_2; Hacker et al., 2015; Rudnick & Gao, 2003).

Our combined petrophysical and petrological analysis and its comparison to geophysical models proposes a mafic signature of the IGB (3–50 km below Valsesia) formed by amphibole gabbros with abundant plagioclase in the upper IGB (3–20 km depth) *and* pyroxene hornblendites with clinopyroxene and limited presence of garnet in the lower IGB (20–50 km depth; Figures 5 and 6). We suggest that the IGB still preserves the structure and composition forged during magmatic underplating (Voshage et al., 1990) ~316-275 million years ago (Klötzli et al., 2014; Peressini et al., 2007) from hydrous magmas (Müntener et al., 2001), containing plagioclase stable to large paleo-depths of up to ~45–50 km, with a resulting crust exceeding the average crustal thickness (~35 km; Christensen & Mooney, 1995; Figure 8). The preservation of such a structure against possible delamination processes is explained by the low density of amphibole gabbros compared to mantle peridotites and pyroxenites (cf. Figure 5c). The seismic signature of the IVZ + upper IGB section is consistent with that of the mafic oceanic crust (Calvert, 2011), that of the continental and oceanic paleo-island arcs (Behn & Kelemen, 2006; Guo et al., 2020; Jagoutz & Behn, 2013; Tibaldi et al., 2013), and that of embryonal continental crust produced at volcanic arcs (Shillington et al., 2004) (Figure 5b). But the pyroxene hornblendites contain sufficient amounts of garnet and clinopyroxene to contribute to the positive gravity anomaly (Figure 2) and could represent the hidden cumulate fraction of the IVZ sequence (~32 km thick; Figures 6 and 8), in line with experimental observations of cumulate line of descent produced by fractional crystallization of hydrous magmas (Müntener & Ulmer, 2018; Ulmer et al., 2018). In our thermodynamic modeling, garnet is limited (<3 vol.%) but stable in an extended paleo-pressure starting from 0.8 GPa in hydrous systems and clinopyroxene along with amphibole are the main mineral phases (Table 2; Figure 6) that produce a relatively high velocity gradient in the depth range of lower IGB (Figure 5b). In the light of our thermodynamic calculations, our results favor a hydrous mantle source to account for the large volumes of amphibole gabbros, composing ~18 km of the upper IGB crustal section, including ~2 km amphibole gabbro unit of the exposed IVZ section (Lu et al., 1997a, 1997b), and pyroxene hornblendites composing the ~32 km thick cumulate body. We propose that a relatively hydrous source was most likely established during subduction processes related to the late stage of the precursor Variscan orogeny (Berno et al., 2020). The thickness of the magmatic additions may be larger, which necessitates reevaluation of the rates of magma production and differentiation in the continental crust.

We note that the currently available geophysical constraints do not allow for a fully self-consistent determination of the internal architecture and physical properties of the IGB. Ongoing seismic investigations at a higher spatial resolution than currently available (Greenwood et al., 2018; Hetényi et al., 2017; Scarponi et al., 2017), especially planned active seismic surveys in Valsesia, will hopefully fill the remaining data gap in terms of V_P contrast and ρ distribution of the IGB and better characterize the shallower part of the IGB. Given the extensive surface exposure of the crustal section and the proximity of the source causing the

geophysical anomalies, the IVZ remains a primary research target. Current efforts aim at assembling data on the deep continental crust and the Moho transition zone and testing several hypotheses of formation, evolution, and modification of the continental lithosphere through space and time. Forthcoming investigations related to the DIVE (Drilling the Ivrea-Verbano zonE) ICDP initiative (Pistone et al., 2017) will address these questions across scales and provide further insights into the properties of the continental lower crust.

Data Availability Statement

All data generated in this study are summarized in Tables 1 and 2 available in the public domain data repository https://doi.org/10.5281/zenodo.4247516 here reported: https://zenodo.org/record/4247516#. X6QjdttCdYg.

References

Abers, G. A., & Hacker, B. R. (2016). A MATLAB toolbox and Excel workbook for calculating the densities, seismic wave speeds, and major element composition of minerals and rocks at pressure and temperature. *Geochemistry, Geophysics, Geosystems*, *17*, 616–624. https://doi.org/10.1002/2015GC006171.

Almqvist, B. S. G., & Mainprice, D. (2017). Seismic properties and anisotropy of the continental crust: Predictions based on mineral texture and rock microstructure. *Reviews of Geophysics*, *55*, 367–433. https://doi.org/10.1002/2016RG000552

Ansorge, J. (1968). Die Struktur der Erdkruste an der Westflanke der Zone von Ivrea. *Schweizerische Mineralogische und Petrographische Mitteilungen*, *48*, 247–254.

Ansorge, J., Mueller, S., Kissling, E., Guerra, I., Morelli, C., & Scarascia, S. (1979). Crustal section across the zone of Ivrea-Verbano from the Valais to the Lago Maggiore. *Bollettino di Geofisica Teorica ed Applicata*, *83*, 149–157.

Babuska, V., Fiala, J., Kumazawa, M., Ohno, I., & Sumino, Y. (1978). Elastic properties of garnet solid-solution series. *Physics of the Earth and Planetary Interiors*, *16*, 157–176.

Barberini, V., Burlini, L., & Zappone, A. S. (2007). Elastic properties, fabric and seismic anisotropy of amphibolites and their contribution to the lower crust reflectivity. *Tectonophysics*, *445*, 227–244.

Barruol, G., & Kern, H. (1996). Seismic anisotropy and shear-wave splitting in lower-crustal and upper-mantle rocks from the Ivrea zone: Experimental and calculated data. *Physics of the Earth and Planetary Interiors*, *95*, 175–194.

Barruol, G., & Mainprice, D. (1993). 3-D seismic velocities calculated from lattice-preferred orientation and reflectivity of a lower crustal section: Examples of the Val sesia section (Ivrea zone, northern Italy). *Geophysical Journal International*, *115*, 1169–1188.

Behn, M. D., & Kelemen, P. B. (2003). Relationship between seismic P-wave velocity and the composition of anhydrous igneous and meta-igneous rocks. *Geochemistry, Geophysics, Geosystems*, *4*, 1041. https://doi.org/10.1029/2002GC000393

Behn, M. D., & Kelemen, P. B. (2006). Stability of arc lower crust: Insights from the Talkeetna arc section, south central Alaska, and the seismic structure of modern arcs. *Journal of Geophysical Research*, *111*, B11207. https://doi.org/10.1029/2006JB004327

Berckhemer, H. (1968). Topographie des "Ivrea-Körpers" abgeleitet aus seismischen und gravimetrischen Daten. *Schweizerische Mineralogische und Petrographische Mitteilungen*, *48*, 235–246.

Berckhemer, H. (1969). Direct evidence for the composition of the lower crust and the Moho. *Tectonophysics*, *8*, 97–105.

Berno, D., Tribuzio, R., Zanetti, A., & Hémond, C. (2020). Evolution of mantle melts intruding the lowermost continental crust: Constraints from the Monte Capio–Alpe Cevia mafic–ultramafic sequences (Ivrea–Verbano Zone, northern Italy). *Contributions to Mineralogy and Petrology*, *175*, 2. https://doi.org/10.1007/s00410-019-1637-8

Bertotti, G. (1991). Early Mesozoic extension and Alpine shortening in the western Southern Alps: The geology of the area between Lugano and Menaggio (Lombardy, northern Italy). In *Memorie di scienze geologiche* (Vol. 43, pp. 17–123). Padova, Italy.

Bertotti, G., Picotti, V., Bernoulli, D., & Castellarin, A. (1993). From rifting to drifting: Tectonic evolution of the South-Alpine upper crust from the Triassic to the Early Cretaceous. *Sedimentary Geology*, *86*, 53–76.

Béthoux, N., Sue, C., Paul, A., Virieux, J., Fréchet, J., Thouvenot, F., & Cattaneo, M. (2007). Local tomography and focal mechanisms in the south-western Alps: Comparison of methods and tectonic implications. *Tectonophysics*, *432*, 1–19.

Birch, F. (1960). The velocity of compressional waves in rocks to 10 kilobars, l. *Journal of Geophysical Research*, *65*, 1083–1102.

Birch, F. (1961). The velocity of compressional waves in rocks to 10 kilobars, 2. *Journal of Geophysical Research*, *66*, 2199–2224.

Boriani, A., & Sacchi, R. (1973). Geology of the junction between the Ivrea-Verbano and strona-Ceneri Zones (southern Alps). In *Memorie degli Istituti di geologia e mineralogia dell'Università di Padova* (Vol. 28, pp. 1–36).

Bowes, D. R. (1989). MohoroviČiĆ discontinuity (moho). In *Petrology. Encyclopedia of Earth science*. Boston, MA: Springer. https://doi.org/10.1007/0-387-30845-8_156

Brack, P., Ulmer, P., & Schmid, S. (2010). A crustal magmatic system from Earth mantle to the Permian surface: Field trip to the area of lower Valsesia and val d'Ossola (Massiccio dei Laghi, Southern Alps, Northern Italy). *Swiss Bulletin for Applied Geology*, *15/2*, 3–21.

Brodie, K. H., & Rutter, E. H. (1987). Deep crustal extensional faulting in the Ivrea zone (N-Italy). *Tectonophysics*, *140*, 193–212.

Brooks, M. (1970). Positive Bouger anomalies in some orogenic belts. *Geological Magazine*, *107*, 399–400.

Burg, J.-P., Bodinier, J.-L., Chaudhry, S., Hussain, S., & Dawwod, H. (1998). Infra-arc mantle–crust transition and intra-arc mantle diapirs in the Kohistan Complex (Pakistani Himalaya): Petrostructural evidence. *Terra Nova*, *102*, 74–80.

Burke, M. M., & Fountain, D. M. (1990). Seismic properties of rocks from an exposure of extended continental crust: New laboratory measurements from the Ivrea Zone. *Tectonophysics*, *182*, 119–146.

Bürki, B. (1990). Geophysical interpretation of astrogravimetric data in the Ivrea Zone: Exposed cross-sections of the continental crust. In M. H. Salisbury & D. M. Fountain (Eds.), *Exposed Cross-Sections of the Continental Crust* NATO ASI Series (Series C: Mathematical and Physical Sciences) (Vol. 317, pp. 545–561). Dordrecht, The Netherlands: Springer.

Burlini, L., & Fountain, D. M. (1993). Seismic anisotropy of metapelites from the Ivrea-Verbano zone and Serie dei Laghi (N. Italy). *Physics of the Earth and Planetary Interiors*, *78*, 301–317.

Calvert, A. J. (2011). The seismic structure of island arc crust. In D. Brown, & P. D. Ryan (Eds.), *Arc-continent collision* (pp. 87–119. Frontiers in Earth Science.

Carlson, R. L., & Miller, D. J. (2003). Mantle wedge water contents estimated from seismic velocities in partially serpentinized peridotites. *Geophysical Research Letters*, *30*, 1250. https://doi.org/10.1029/2002GL016600

Cawthorn, R. G. (1975). The amphibole peridotite-metagabbro complex, Finero, Northern Italy. *The Journal of Geology*, *83*, 437–454.

Christensen, N. I. (1966). Eladticity of ultrabasic rocks. *Journal of Geophysical Research*, *71*, 5921–5931.

Christensen, N. I., & Mooney, W. D. (1995). Seismic velocity structure and composition of the continental crust: A global view. *Journal of Geophysical Research*, *100*(B6), 9761–9788.

Coltorti, M., & Siena, F. (1984). Mantle tectonite and fractionate peridotite at Finero (Italian Western Alps). *Neues Jahrbuch für Mineralogie*, *149*, 225–244.

Connolly, J. A. D. (1990). Multivariable phase-diagrams: An algorithm based on generalized thermodynamics. *American Journal of Science*, *290*, 666–718.

Connolly, J. A. D. (2005). Computation of phase equilibria by linear programming: A tool for geodynamic modeling and its application to subduction zone decarbonation. *Earth and Planetary Science Letters*, *236*, 524–541.

Connolly, J. A. D. (2009). The geodynamic equation of state: What and how. *Geochemistry, Geophysics, Geosystems*, *10*, Q10014. https://doi.org/10.1029/2009GC002540

Connolly, J. A. D., & Petrini, K. (2002). An automated strategy for calculation of phase diagram sections and retrieval of rock properties as a function of physical conditions. *Journal of Metamorphic Geology*, *20*, 697–708.

Dale, J., Holland, T. J. B., & Powell, R. (2000). Hornblende-garnet-plagioclase thermobarometry: A natural assemblage calibration of the thermodynamics of hornblende. *Contributions to Mineralogy and Petrology*, *140*, 353–362.

de Franco, R., Biella, G., Boniolo, G., Corsi, A., Demartin, M., Maistrello, M., & Morrone, A. (1997). Ivrea seismic array: A study of continental crust and upper mantle. *Geophysical Journal International*, *128*, 723–736.

Demarchi, G., Quick, J. E., Sinigoi, S., & Mayer, A. (1998). Pressure gradient and original orientation of a lower-crustal intrusion in the Ivrea-Verbano Zone, Northern Italy. *The Journal of Geology*, *106*, 609–622.

Diehl, T., Husen, S., Kissling, E., & Deichmann, N. (2009). High resolution 3-D P-wave model of the Alpine crust. *Geophysical Journal International*, *179*, 1133–1147.

Ewing, T. A., Rubatto, D., Beltrando, M., & Hermann, J. (2015). Constraints on the thermal evolution of the Adriatic margin during Jurassic continental break-up: U-Pb dating of rutile from the Ivrea-Verbano Zone, Italy. *Contributions to Mineralogy and Petrology*, *169*, 44.

Ewing, T. A., Rubatto, D., & Hermann, J. (2013). The robustness of the Zr-in rutile and Ti-in-zircon thermometers during high-temperature metamorphism (Ivrea-Verbano Zone, Northern Italy). *Contributions to Mineralogy and Petrology*, *165*, 757–779.

Forman, D. J., & Shaw, R. D. (1973). Deformation of the crust and mantle in central Australia. *Bureau of Mineral Resources Geology and Geophysics Bulletin*, *144*, 20.

Fountain, D. M. (1976). The Ivrea—Verbano and Strona-Ceneri Zones, Northern Italy: A cross-section of the continental crust—New evidence from seismic velocities of rock samples. *Tectonophysics*, *33*, 145–165.

Fountain, D. M. (1989). Growth and modification of lower continental crust in extended terrains: The role of extension and magmatic underplating. In R. F. Mereu, S. Mueller, & D. M. Fountain (Eds.), Properties and processes of Earth's lower crust (Vol. 51, pp. 287–299). Washington, DC: AGU.

Fountain, D. M., Salisbury, M. H., & Percival, J. A. (1990). Seismic structure of the continental crust based on rock velocity measurements from the Kapuskasing uplift. *Journal of Geophysical Research*, *95*, 1167–1186.

Gansser, A. (1968). The Insubric Line, a major geotectonic problem. *Schweizerische Mineralogische und Petrographische Mitteilungen*, *48*, 123–144.

Gibb, R. A., & Thomas, M. D. (1976). Gravity signature of fossil plate boundaries in the Canadian Shield. *Nature*, *262*, 199–200.

Godovikov, A. A., & Kennedy, G. C. (1968). Kyanite eclogites. *Contributions to Mineralogy and Petrology*, *19*, 169–176.

Greenwood, A., Baron, L., Merz, K., Langone, A., Petri, B., Kard, A. O., et al. (2018). *High-resolution seismic reflection survey across the Insubric Line*. Paper presented at 8th International Conference on Environmental and Engineering Geophysics, Hangzhou, China, Italian Alps.

Grieco, G., Ferrario, A., Von Quadt, A., Koeppel, V., & Mathez, E. A. (2001). The zircon-bearing chromitites of the phlogopite peridotite of Finero (Ivrea zone, Southern Alps): Evidence and geochronology of a metasomatized mantle slab. *Journal of Petrology*, *42*, 89–101.

Guo, L., Jagoutz, O., Shinevar, W. J., & Zhang, H.-F. (2020). Formation and composition of the Late Cretaceous Gangdese arc lower crust in southern Tibet. *Contributions to Mineralogy and Petrology*, *175*, 58. https://doi.org/10.1007/s00410-020-01696-y

Hacker, B. R., & Abers, G. A. (2004). Subduction Factory 3: An Excel worksheet and macro for calculating the densities, seismic wave speeds, and H_2O contents of minerals and rocks at pressure and temperature. *Geochemistry, Geophysics, Geosystems*, *5*, Q01005. https://doi.org/10.1029/2003GC000614

Hacker, B. R., Kelemen, P. B., & Behn, M. D. (2015). Continental lower crust. *Annual Review of Earth and Planetary Sciences*, *43*, 167–205. https://doi.org/10.1146/annurev-earth-050212-124117

Handy, M. R. (1987). The structure, age and kinematics of the Pogallo Fault Zone, Southern Alps, northwestern Italy. *Eclogae Geologicae Helvetiae*, *80*, 593–632.

Handy, M., Franz, L., Heller, F., Janott, B., & Zurbriggen, R. (1999). Multistage accretion and exhumation of the continental crust (Ivrea crustal section, Italy and Switzerland). *Tectonics*, *18*, 1154–1177.

Handy, M. R., & Zingg, A. (1991). The tectonic and rheological evolution of an attenuated cross-section of the continental crust: Ivrea crustal section, southern Alps, northwestern Italy and southern Switzerland. *The Geological Society of America Bulletin*, *103*, 236–253.

Hartmann, G., & Wedepohl, K. H. (1993). The composition of peridotite tectonites from the Ivrea Complex, northern Italy: Residues from melt extraction. *Geochimica et Cosmochimica Acta*, *57*, 1761–1782.

Henk, A., Franz, L., Teufel, S., & Oncken, O. (1997). Magmatic underplating, extension, and crustal reequilibration: Insights from a cross-section through the Ivrea Zone and Strona-Ceneri Zone, N-Italy. *The Journal of Geology*, *105*, 367–377.

Hetényi, G., Plomerová, J., Solarino, S., Scarponi, M., Vecsey, L., Munzarová, H, et al. (2017). IvreaArray—An AlpArray complementary experiment. *Zenodo*. https://doi.org/10.5281/zenodo.1038209

Hodges, K. V., & Fountain, D. M. (1984). Pogallo line, south Alps, Northern Italy—An intermediate low angle normal fault. *Geology*, *12*, 151–155.

Holland, T. J. B. (1980). The reaction albite = jadeite * quartz determined experimentally in the range 600-1200°C. *American Mineralogist*, *65*, 129–134.

Holland, T. J. B., & Powell, R. (1996). Thermodynamics of order-disorder in minerals. 2. Symmetric formalism applied to solid solutions. *American Mineralogist*, *81*, 1425–1437.

Holland, T. J. B., & Powell, R. T. J. B. (1998). An internally consistent thermodynamic data set for phases of petrological interest (version 2002). *Journal of Metamorphic Geology*, *16*, 309–343.

Holland, T. J. B., & Powell, R. (2003). Activity-composition relations for phases in petrological calculations: An asymmetric multicomponent formulation. *Contributions to Mineralogy and Petrology*, *145*, 492–501.

Jagoutz, O. (2014). Arc crustal differentiation mechanisms. *Earth and Planetary Science Letters*, *396*, 267–277.

Jagoutz, O., & Behn, M. D. (2013). Foundering of lower island-arc crust as an explanation for the origin of the continental Moho. *Nature*, *504*, 131–134.

James, T. (2001). *A study of the geological structure of the Massiccio dei Laghi (Northern Italy)* (Unpublished PhD thesis): University of Manchester.

Jamieson, H. E., & Roeder, P. L. (1984). The distribution of Mg and Fe-2+ between olivine and spinel at 1300°C. *American Mineralogist*, *69*, 283–291.

Jerauld, G. R., & Salter, S. J. (1990). The effect of pore-structure on hysteresis in relative permeability and capillary pressure: Pore-level modelling. *Transport in Porous Media*, *5*, 103–151.

Kästle, E. D., El-Sharkawy, A., Boschi, L., Meier, T., Rosenberg, C., Bellahsen, N., et al. (2018). Surface wave tomography of the Alps using ambient-noise and earthquake phase velocity measurements. *Journal of Geophysical Research: Solid Earth*, *123*, 1770–1792. https://doi.org/10.1002/2017JB014698

Khazanehdari, J., Rutter, E. H., & Brodie, K. H. (2000). High pressure/temperature seismic velocity structure of the mid- and lower-crustal rocks of the Ivrea-Verbano zone and Serie dei Laghi, NW Italy. *Journal of Geophysical Research*, *105*, 13843–13858.

Kissling, E. (1980). *Krustenaufbau und Isostasie in der Schweiz* (PhD Dissertation, p. 165). Zurich, Switzerland: ETH-Zurich.

Kissling, E. (1984). Three dimensional gravity model of the northern Ivrea-Verbano zone. In J. J. Wagner, & S. Mueller (Eds.), *Geomagnetic and gravimetric studies of the Ivrea zone* (pp. 53–61). Neuchâtel, Switzerland: Swiss Geophysical Commission, Kümmerly & Frey.

Kissling, E. (1993). Deep structure of the Alps: What do we really know? *Physics of the Earth and Planetary Interiors*, *79*, 87–112.

Klötzli, U. S., Sinigoi, S., Quick, J. E., Demarchi, G., Tassinari, C. C. G., Sato, K., & Günes, Z. (2014). Duration of igneous activity in the Sesia Magmatic System and implications for high-temperature metamorphism in the Ivrea-Verbano deep crust. *Lithos*, *206–207*, 19–33.

Lanza, R. (1982). Models for interpretation of the magnetic anomaly of the Ivrea body. *Geologie Alpine*, *58*, 85–94.

Lombardi, D., Braunmiller, J., Kissling, E., & Giardini, D. (2008). Moho depth and Poisson's ratio in the Western-Central Alps from receiver functions. *Geophysical Journal International*, *173*, 249–264.

Lu, M., Hofmann, A. W., Mazzucchelli, M., & Rivalenti, G. (1997a). The mafic-ultramafic complex near Finero Ivrea-Verbano Zone: I. Chemistry of MORB-like magmas. *Chemical Geology*, *140*, 207–222.

Lu, M., Hofmann, A. W., Mazzucchelli, M., & Rivalenti, G. (1997b). The mafic-ultramafic complex near Finero (Ivrea-Verbano Zone), II. Geochronology and isotope geochemistry. *Chemical Geology*, *140*, 223–235.

Lu, Y., Stehly, L., & Paul, A. (2018). High-resolution surface wave tomography of the Europeancrust and uppermost mantle from ambient seismic noise. *Geophysical Journal International*, *214*, 1136–1150.

Masson, F., Verdun, J., Bayer, R., & Debeglia, N. (1999). Une nouvelle cartegravimétrique des Alpes occidentales et ses conséquences structurales et tectoniques. *Comptes Rendus de l'Académie des Sciences—Series IIA—Earth and Planetary Science*, *329*, 865–871.

Mazzucchelli, M., Rivalenti, G., Brunelli, D., Zanetti, A., & Boari, E. (2009). Formation of highly refractory dunite by Focused Percolation of pyroxenite-derived Melt in the Balmuccia peridotite Massif (Italy). *Journal of Petrology*, *50*, 1205–1233.

Mazzucchelli, M., Zanetti, A., Rivalenti, G., Vannucci, R., Correia, C. T., & Gaeta Tassinari, C. C. (2010). Age and geochemistry of mantle peridotites and diorite dykes from the Baldissero body: Insights into the Paleozoic-Mesozoic evolution of the Southern Alps. *Lithos*, *119*, 485–500.

Ménard, G., & Thouvenot, P. (1984). Ecaillage de la lithosphère européenne sous les Alpes Occidentales; arguments gravimétriques et sismiques liés à l'anomalie d'Ivrea. *Bulletin de la Societe Geologique de France*, *26*, 875–884.

Miller, D. J., & Christensen, N. I. (1997). *Seismic velocities of lower crustal and upper mantle rocks from the slow-spreading Mid-Atlantic Ridge, south of the Kane Fracture Zone (MARK)* (pp. 437–454). Proceedings of the Ocean Drilling Program—Scientific Results.

Mohorovičić, A. (1910). *Epicenters of earthquakes in Croatia and slavonia* (Yearly Report of the Zagreb Meteorological Observatory for the Year 1909).

Molinari, I., Verbeke, J., Boschi, L., Kissling, E., & Morelli, A. (2015). Italian and Alpine three-dimensional crustal structure imaged by ambient-noise surface-wave dispersion. *Geochemistry, Geophysics, Geosystems*, *16*, 4405–4421. https://doi.org/10.1002/2015GC006176

Mukasa, S. B., & Shervais, J. W. (1999). Growth of subcontinental lithosphere: Evidence from repeated dike injections in the Balmuccia Iherzolite Massif, Italian Alps. *Developments in Geotectonics*, *24*, 287–316.

Mulch, A., Rosenau, M., Dörr, W., & Handy, M. (2002). The age and structure of dikes along the tectonic contact of the Ivrea-Verbano and strona-Ceneri Zones (Southern Alps, Northern Italy, Switzerland). *Schweizerische Mineralogische und Petrographische Mitteilungen*, *82*, 55–76.

Müntener, O., Hermann, J., & Trommsdorff, V. (2000). Cooling history and exhumation of lower-crustal granulite and upper mantle (Malenco, Eastern Central Alps). *Journal of Petrology*, *41*, 175–200.

Müntener, O., Kelemen, P. O., & Grove, T. L. (2001). The role of H_2O during crystallization of primitive arc magmas under uppermost mantle conditions and genesis of igneous pyroxenites: An experimental study. *Contributions to Mineralogy and Petrology*, *141*, 643–658.

Müntener, O., & Ulmer, P. (2006). Experimentally derived high-pressure cumulates from hydrous arc magmas and consequences for the seismic velocity structure of lower arc crust. *Geophysical Research Letters*, *33*, L21308. https://doi.org/10.1029/2006GL027629

Müntener, O., & Ulmer, P. (2018). Arc crust formation and differentiation constrained by experimental petrology. *American Journal of Science*, *318*, 64–89

Nafe, J. E., & Drake, C. L. (1957). Variation with depth in shallow and deep water marine sediments of porosity, density and the velocities of compressional and shear waves. *Geophysica Norvegica*, *22*, 523–552.

Nicolas, A., Hirn, A., Nicolich, R., & Polino, R., & ECORS-CROP Working Group. (1990). Lithospheric wedging in the Western Alps inferred from the ECORS-CROP traverse. *Geology*, *18*, 587–590.

Niggli, E. (1946). Über den Zusammenhang zwischen der positiven Schwereanomalie am Südfuß der Westalpen und der Gesteinszone von Ivrea. *Eclogae Geologicae Helvetiae*, *39*, 211–220.

Paul, A., Cattaneo, M., Thouvenot, F., Spallarossa, D., Béthoux, N., & Fréchet, J. (2001). A three-dimensional crustal velocity model of the south-western Alps from local earthquake tomography. *Journal of Geophysical Research*, *106*, 19367–19389.

Percival, J. A., Fountain, D. M., & Salisbury, M. H. (1992). Exposed crustal cross sections as windows on the lower crust. In D. M. Fountain, R. Arculus, & R. W. Kay (Eds.), *Continental lower crust: Developments in geotectonics* (pp. 317–362). Amsterdam, The Netherlands: Elsevier.

Peressini, G., Quick, J. E., Sinigoi, S., Hofmann, A. W., & Fanning, M. (2007). Duration of a large mafic intrusion and heat transfer in the lower crust: A SHRIMP U–Pb zircon study in the Ivrea–Verbano Zone (Western Alps, Italy). *Journal of Petrology*, *48*, 1185–1218.

Petri, B., Duretz, T., Mohn, G., Schmalholz, S., Karner, G., & Müntener, O. (2019). Thinning mechanisms of heterogeneous continental lithosphere. *Earth and Planetary Science Letters*, *512*, 147–162.

Petri, B., Mohn, G., Skrzypek, E., Mateeva, T., Galster, F., & Manatschal, G. (2017). U–Pb geochronology of the Sondalo gabbroic complex (Central Alps) and its position within the Permian post-Variscan extension. *International Journal of Earth Sciences*, *106*, 2873–2893.

Petri, B., Mohn, G., Štípská, P., Schulmann, K., & Manatschal, G. (2016). The sondalo gabbro contact aureole (Campo unit, Eastern Alps): Implications for mid-crustal mafic magma emplacement. *Contributions to Mineralogy and Petrology*, *171*, 52. https://doi.org/10.1007/s00410-016-1263-7

Pin, C., & Sills, J. D. (1986). Petrogenesis of layered gabbros and ultramafic rocks from Val sesia, the Ivrea Zone, NW Italy. In J. B. Dawson, D. A. Carswell, J. Hall, & K. H. Wedepohl (Eds.), *The nature of the lower continental crust* (Vol. 24, pp. 231–249) Geological Society.

Pistone, M., Müntener, O., Ziberna, L., Hetényi, G., & Zanetti, A. (2017). Report on the ICDP workshop DIVE (drilling the Ivrea–Verbano zone). *Scientific Drilling*, *23*, 47–56.

Quick, J. E., Sinigoi, S., & Mayer, A. (1995). Emplacement of mantle peridotite in the lower continental crust, Ivrea-Verbano Zone, northwest Italy. *Geology*, *23*, 739–742.

Quick, J. E., Sinigoi, S., Snoke, A. W., Kalakay, T. J., Mayer, A., & Peressini, G. (2003). *Geologic map of the southern Ivrea-Verbano Zone, Northwestern Italy*. Reston, Virgina, VA: USGS.

Redler, C., Johnson, T., White, R., & Kunz, B. (2012). Phase equilibrium constraints on a deep crustal metamorphic field gradient: Metapelitic rocks from the Ivrea Zone (NW Italy). *Journal of Metamorphic Geology*, *3*, 235–254.

Rey, D. (1990). Gravity and aeromagnetic maps of the western Alps: Contribution to the knowledge of the deep structures along the ECORS-CROP seismic profile. *Mémoires de la Société géologique de France*, *156*, 107–121.

Rivalenti, G., Garuti, G., & Rossi, A. (1975). The origin of the Ivrea-Verbano basic formation (western Italian Alps): Whole rock geochemistry. *Bollettino della Società Geologica Italiana*, *94*, 1149–1186.

Rivalenti, G., Mazzucchelli, M., Vannucci, R., Hofmann, A. W., Ottolini, L., Bottazzi, P., & Obermiller, W. (1995). The relationship between websterite and peridotite in the Balmuccia peridotite Massif, NW Italy, as revealed by trace element variations in clinopyroxene. *Contributions to Mineralogy and Petrology*, *121*, 275–288.

Rudnick, R. L., & Fountain, D. M. (1995). Nature and composition of the continental crust: A lower crustal perspective. *Reviews of Geophysics*, *33*, 267–309.

Rudnick, R. L., & Gao, S. (2003). The composition of the continental crust. In R. L. Rudnick (Ed.), *The crust* (pp. 1–64). Oxford, UK: Elsevier-Pergamon.

Rudnick, R. L., & Presper, T. (1990). Geochemistry of intermediate to high-pressure granulites. In D. Vielzeuf & P. Vidal (Eds.), *Granulites and crustal evolution* (pp. 523–550). Norwell, MA: Kluwer Acad.

Rutter, E., Brodie, K., James, T., Blundell, D. J., & Waltham, D. A. (2003). Seismic modeling of lower and mid-crustal structure as exemplified by the Massiccio dei Laghi (Ivrea-Verbano Zone and Serie dei Laghi) Crustal Section, Northwestern Italy. In J. A. Goff, & K. Holliger (Eds.), *Heterogeneity in the crust and upper mantle* (pp. 67–97). Kluwer Academic/Plenum Publishers.

Salisbury, M. H., & Fountain, D. M. (Eds.). (1990). *Exposed cross-sections of the continental crust* (NATO ASI Series C, Vol. 317). Dordrecht, The Netherlands and Boston, MA and London, UK: Kluwer.

Sanders, C. A. E., Bertotti, G., Tommasini, S., Davies, G. R., & Wijbrans, J. R. (1996). Triassic pegmatites in the Mesozoic middle crust of the Southern Alps (Italy): Fluid inclusions, radiometric dating and tectonic implications. *Eclogae Geologicae Helvetiaa*, *89*, 505–525.

Scarponi, M., Hetényi, G., Berthet, T., Baron, L., Manzotti, P., Petri, B., et al. (2020). New gravity data and 3D density model constraints on the Ivrea geophysical body (Western Alps). *Geophysical Journal International*, *222*, 1977–1991. https://doi.org/10.1093/gji/ggaa263

Scarponi, M., Hetényi, G., Plomerová, J., Solarino, S., Berthet, T., & Baron, L. (2017). *High-resolution imaging of the Ivrea geophysical body: A receiver function and gravity approach*. Paper presented at 15th Swiss Geoscience Meeting, Switzerland, Davos.

Schaltegger, U., & Brack, P. (2007). Crustal-scale magmatic systems during intracontinental strike-slip tectonics: U, Pb and Hf isotopic constraints from permian magmatic rocks (S-Alps). *International Journal of Earth Sciences*, *96*, 1131–1151.

Schaltegger, U., Ulianov, A., Müntener, O., Ovtcharova, M., Peytcheva, I., Vonlanthen, P., et al. (2015). Megacrystic zircon with planar fractures in miaskite-type nepheline pegmatites formed at high pressures in the lower crust (Ivrea Zone, Southern Alps, Switzerland). *American Mineralogist*, *100*, 83–94.

Schmid, S. M., Fügenschuh, B., Kissling, E., & Schuster, R. (2004). Tectonic map and overall architecture of the Alpine orogen. *Eclogae Geologicae Helvetiae*, *97*, 93–117.

Schmid, S. M., & Kissling, E. (2000). The arc of the Western Alps in the light of geophysical data on deep crustal structure. *Tectonics*, *19*, 62–85.

Schmid, S. M., Kissling, E., Diehl, T., van Hinsbergen, D. J. J., & Molli, G. (2017). Ivrea mantle wedge, arc of the Western Alps, and kinematic evolution of the Alps-Appenines orogenic system. *Swiss Journal of Geosciences*, *110*, 581–612. https://doi.org/10.1007/s00015-016-0237-0

Schmid, S. M., Zingg, A., & Handy, M. (1987). The kinematics of movements along the Insubric Line and the emplacement of the Ivrea Zone. *Tectonophysics*, *135*, 47–66.

Schuster, R., & Stüwe, K. (2008). Permian metamorphic event in the Alps. *Geology*, *36*, 603–606.

Shervais, J. W., & Mukasa, S. B. (1991). The Balmuccia orogenic lherzolite massif, Italy. *Journal of Petrology*, *2*, 155–174.

Shillington, D. J., Van Avendonk, H. J. A., Holbrook, W. S., Kelemen, P. B., & Hornbach, M. J. (2004). Composition and structure of the central Aleutian island arc from arc-parallel wide-angle seismic data. *Geochemistry, Geophysics, Geosystems*, *5*, Q10006. https://doi.org/10.1029/2004GC000715

Siegesmund, S., Layer, P., Dunkl, I., Vollbrecht, A., Steenken, A., Wemmer, K., & Ahrendt, H. (2008). Exhumation and deformation history of the lower crustal section of the Valstrona di Omegna in the Ivrea Zone, southern Alps. In Tectonic aspects of the Alpine-Dinaride-Carpathian system (Vol. 298, pp. 45–68): Geological Society of London.

Siena, F., & Coltorti, M. (1989). The petrogenesis of a hydrated mafic-ultramafic complex and the role of amphibole fractionation at Finero (Italian Western Alps). *Neues Jahrbuch für Mineralogie*, *6*, 255–274.

Sinigoi, S., Antonini, P., Demarchi, G., Longinelli, A., Mazzucchelli, M., Negrini, L., & Rivalenti, G. (1991). Interactions of mantle and crustal magmas in the southern part of the Ivrea Zone (Italy). *Contributions to Mineralogy and Petrology*, *108*, 385–395.

Sinigoi, S., Quick, J. E., Demarchi, G., & Klötzli, U. (2011). The role of crustal fertility in the generation of large silicic magmatic systems triggered by intrusion of mantle magma in the deep crust. *Contributions to Mineralogy and Petrology*, *162*, 691–707.

Smye, A. J., Lavier, L. L., Zack, T., & Stockli, D. F. (2019). Episodic heating of continental lower crust during extension: A thermal modeling investigation of the Ivrea-Verbano Zone. *Earth and Planetary Science Letters*, *521*, 158–168.

Snoke, A. W., Kalakay, T. J., Quick, J. E., & Sinigoi, S. (1999). Development of a deep-crustal shear zone in response to syntectonic intrusion of mafic magma into the lower crust, Ivrea-Verbano Zone, Italy. *Earth and Planetary Science Letters*, *166*, 31–45.

Sobolev, S. V., & Babeyko, A. Y. (1994). Modeling of mineralogical composition, density and elastic wave velocities in anhydrous magmatic rocks. *Surveys in Geophysics*, *15*, 515–544.

Solarino, S., Kissling, E., Cattaneo, M., & Cardillo, E. (1997). Local earthquake tomography of the southern part of the Ivrea body, North-Western Italy. *Eclogae Geologicae Helvetiae*, *90*, 357–364.

Solarino, S., Malusà, M. G., Eva, E., Guillot, S., Paul, A., Schwartz, S., et al. (2018). Mantle wedge exhumation beneath the Dora-Maira (U) HP dome unravelled by local earthquake tomography (Western Alps). *Lithos*, *296*, 623–636.

Spada, M., Bianchi, I., Kissling, E., Piana Agostinetti, N., & Wiemer, S. (2013). Combining controlled-source seismology and receiver function information to derive 3-D Moho topography for Italy. *Geophysical Journal International*, *194*, 1050–1068.

Spicher, A. (Ed.). (1968). Symposium "Zone Ivrea-Verbano". *Schweizerische Mineralogische und Petrographische Mitteilungen*, *48*, 1–355.

Stähle, V., Frenzel, G., & Hess, J. C. (2001). Permian metabasalt and Triassic alkaline dykes in the northern Ivrea zone: Clues to the post-Variscan geodynamic evolution of the Southern Alps. *Schweizerische Mineralogische und Petrographische Mitteilungen*, *81*, 1–21.

Stähle, V., Frenzel, G., Kober, B., Michard, A., Puchelt, H., & Schneider, W. (1990). Zircon syenite pegmatites in the Finero peridotite (Ivrea Zone): Evidence for a syenite from a mantle source. *Earth and Planetary Science Letters*, *101*, 196–205.

Stehly, L., Fry, B., Campillo, M., Shapiro, N. M., Guilbert, J., Boschi, L., & Giardini, D. (2009). Tomography of the Alpine region from observations of seismic ambient noise. *Geophysical Journal International*, *178*, 338–350.

Stixrude, L., & Lithgow-Bertelloni, C. (2011). Thermodynamics of mantle minerals-II. Phase equilibria. *Geophysical Journal International*, *184*, 1180–1213.

The ECORS-CROP Deep Seismic Sounding Group. (1989). Mapping the Moho of the Western Alps by wide-angle reflection seismics. *Tectonophysics*, *162*, 193–202.

The ECORS-CROP Gravity Group. (1989). Gravity modelling along the ECORS-CROP vertical seismic reflection profile through the Western Alps. *Tectonophysics*, *162*, 203–218.

Thouvenot, F., Paul, A., Fréchet, J., Béthoux, N., Jenatton, L., & Guiguet, R. (2007). Are there really superposed Mohos in the southwestern Alps? New seismic data from fan profiling reflections. *Geophysical Journal International*, *170*, 1180–1194.

Tibaldi, A. M., Otamendi, J. E., Cristofolini, E. A., Baliani, I., Walker, B. A., & Bergantz, G. W. (2013). Reconstruction of the Early Ordovician Famatinian arc through thermobarometry in lower and middle crustal exposures, Sierra de Valle Fértil, Argentina. *Tectonophysics*, *589*, 151–166. https://doi.org/10.1016/j.tecto.2012.12.032.

Tommasi, A., Langone, A., Padrón-Novarta, J. A., Zanetti, A., & Vauchez, A. (2017). Hydrous melts weaken the mantle, crystallization of pargasite and phlogopite does not: Insights from a petrostructural study of the Finero peridotites, southern Alps. *Earth and Planetary Science Letters*, *477*, 59–72.

Ulmer, P., Kaegi, R., & Müntener, O. (2018). Experimentally derived intermediate to silica-rich arc magmas by fractional and equilibrium crystallization at 1.0 GPa: An evaluation of phase relationships, compositions, liquid lines of descent and oxygen fugacity. *Journal of Petrology*, *59*, 11–58.

Vecchia, O. (1968). La zone Cuneo-Ivrea-Locarno, élément fondamental des Alpes. Géophysique et géologie. *Schweizerische Mineralogische und Petrographische Mitteilungen*, *48*, 215–226.

Vernant, P., Masson, F., Bayer, R., & Paul, A. (2002). Sequential inversion of local earthquake traveltimes and gravity anomaly: The example of the western Alps. *Geophysical Journal International*, *150*, 79–90.

Veselov, K. E., Galdin, N. E., Karus, E. W., Kuznetsov, O. L., Kuznetsov, Y. I., Litvinenko, I. V., et al. (1987). Vertical zonation in rock physical properties and of the crustal structure from the results of the present study. In Y. A. Kozlovsky (Ed.), *The superdeep well of the Kola Peninsula* (pp. 405–419). Berlin, Germany: Springer.

von Raumer, J. F., Bussy, F., Schaltegger, U., Schulz, B., & Stampfli, G. M. (2013). Pre-Mesozoic Alpine basements: Their place in the European Paleozoic framework. *The Geological Society of America Bulletin*, *125*, 89–108.

Voshage, H., Hofmann, A. W., Mazzucchelli, M., Rivalenti, G., Sinigoi, S., Raczek, I., & Demarchi, G. (1990). Isotopic evidence from the Ivrea Zone for a hybrid lower crust formed by magmatic underplating. *Nature*, *437*, 731–736.

Wagner, A. G., & Reimer, M. G. (1972). Fission track tectonics: The tectonic interpretation of fission track apatite ages. *Earth and Planetary Science Letters*, *14*, 263–268. https://doi.org/10.1016/0012-821X(72)90018-0

Wolff, R., Dunkl, I., Kiesselbach, G., Wemmer, K., & Siegesmund, S. (2012). Thermochronological constraints on the multiphase exhumation history of the Ivrea-Verbano Zone of the Southern Alps. *Tectonophysics*, *579*, 104–117.

Woollard, G. P. (1975). Regional changes in gravity and their relation to crustal parameters. *Bull d'Information*, *36*, 106–110.

Zanetti, A., Mazzucchelli, M., Rivalenti, G., & Vannucci, R. (1999). The Finero phlogopite-peridotite massif: An example of subduction-related metasomatism. *Contributions to Mineralogy and Petrology*, *134*, 107–122.

Zanetti, A., Mazzucchelli, M., Sinigoi, S., Giovanardi, T., Peressini, G., & Fanning, M. (2013). SHRIMP U-Pb Zircon Triassic intrusion age of the Finero Mafic Complex (Ivrea-Verbano Zone, Western Alps) and its geodynamic implications. *Journal of Petrology*, *54*, 2235–2265.

Zappone, A. S. (1994). Calculated and observed seismic behaviour of exposed upper mantle. *Surveys in Geophysics*, *15*, 619–642.

Zappone, A., Morrone, A., Maistrello, M., Demartin, M., de Franco, R., Corsi, A., et al. (1992). *The IGL seismic network in the Ivrea-Verbano zone. Ivrea-Verbano Zone workshop* (Geological Survey Circular 1089, pp. 21–22).

Zhao, L., Paul, A., Guillot, A., Solarino, S., Malusà, M. G., Zheng, T., et al. (2015). First seismic evidence for continental subduction beneath the Western Alps. *Geology*, *43*, 815–818.

Zingg, A. (1983). The Ivrea and Strona-Ceneri Zones (southern Alps, Ticino and N-Italy): A review. *Schweizerische Mineralogische und Petrographische Mitteilungen*, *63*, 361–392.

Zingg, A. (1990). The Ivrea crustal cross-section (Northern Italy and Southern Switzerland). In M. H. Salisbury, & D. M. Fountain (Eds.), *Exposed cross-sections of the continental crust (NATO ASI Series C: Mathematical and Physical Sciences)* (Vol. 317, pp. 1–19). Dordrecht, The Netherlands: Springer.